Tectonics®

RESEARCH ARTICLE
10.1029/2022TC007354

Key Points:

- The Late Triassic granitoids of Southern-Central Chile were emplaced from 220 to 210 Ma
- S, S/I, and A-type granites characterize Late Triassic magmatism
- Slab-tearing was likely the driver for granite generation in Southern-Central Chile

Supporting Information:

Supporting Information may be found in the online version of this article.

Correspondence to:

P. Rossel,
pablo.rossel@unab.cl

Citation:

Rossel, P., Gianni, G. M., Reinoso, V., Fanning, C. M., Ducea, M. N., Muñoz, T., & Salvat, D. (2023). Origin of Late Triassic granitoids of the Coastal Cordillera of Southern Central Chile (34°–37°S): Multi-isotopic evidence of slab tearing effects on pre-Andean magmagenesis. *Tectonics*, *42*, e2022TC007354. https://doi.org/10.1029/2022TC007354

Received 13 APR 2022
Accepted 21 JAN 2023

Author Contributions:

Conceptualization: Pablo Rossel, Guido M. Gianni, Valeria Reinoso, Tamara Muñoz, Daniela Salvat
Formal analysis: C. Mark Fanning
Funding acquisition: Pablo Rossel
Investigation: Pablo Rossel, Guido M. Gianni, Valeria Reinoso, Tamara Muñoz, Daniela Salvat
Methodology: C. Mark Fanning, Mihai N. Ducea
Project Administration: Pablo Rossel
Supervision: Pablo Rossel, C. Mark Fanning, Mihai N. Ducea
Validation: Guido M. Gianni, C. Mark Fanning, Mihai N. Ducea
Writing – original draft: Pablo Rossel, Guido M. Gianni

Origin of Late Triassic Granitoids of the Coastal Cordillera of Southern Central Chile (34°–37°S): Multi-Isotopic Evidence of Slab Tearing Effects on Pre-Andean Magmagenesis

Pablo Rossel[1], Guido M. Gianni[2,3], Valeria Reinoso[1], C. Mark Fanning[4], Mihai N. Ducea[5,6], Tamara Muñoz[1], and Daniela Salvat[1]

[1]Facultad de Ingeniería, Geología, Universidad Andres Bello, Concepcion, Chile, [2]*IGSV*. Instituto Geofísico Sismológico Ing. F. Volponi. Universidad de Nacional San Juan, San Juan, Argentina, [3]Consejo Nacional de Investigaciones Científicas y Técnicas (CONICET), Buenos Aires, Argentina, [4]Research School of Earth Sciences, The Australian National University, Canberra, ACT, Australia, [5]Faculty of Geology and Geophysics, University of Bucharest, Bucharest, Romania, [6]University of Arizona, Tucson, AZ, USA

Abstract The Coastal Cordillera of Central Chile (34°–37°S) holds a series of Late Triassic granitoids classically interpreted as early Andean subduction-related magmatism based on their arc-like geochemical signature. Here, we present geochemical, isotopic, and geochronological data and a tomotectonic analysis that challenge this idea indicating a local interruption of the normal subduction process likely associated with a slab-tearing event. Our results suggest that the source of the magmas is related to melting of asthenospheric mantle and crustal rocks of a metasedimentary Paleozoic complex. We suggest that partial melting of these sources was triggered by a slab tear-related asthenosphere upwelling producing high-silica S/I- and S-Type granites of the Constitución and Hualpén areas, and anorogenic A-Type granitoids in Cobquecura area. Also, partial melting of a metasomatized asthenospheric mantle plus continental crust that experienced previous high-temperature hydrothermal alteration would have generated high-silica magmas with low $\delta^{18}O$, high Pb, CHUR-like $^{87}Sr/^{86}Sr$, and $^{143}Nd/^{144}Nd$ ratios that originated La Estrella Granite. Our results offer an alternative explanation for the existence of subtle magmatic arc-like geochemical signatures in the study area and support a segmentation of the active margin during the Late Triassic. The widespread upper-plate magmatic record of slab-tearing, spanning the Coastal Cordillera of Central Chile to the intraplate Neuquén basin in Argentina, and the lower mantle record of a slab gap, detected in ours and previous tomotectonic analyses, make the Late Triassic slab-tearing event in southwestern Pangea the most robustly constrained pre-Cenozoic slab tear process so far.

1. Introduction

Slab tearing commonly occurs as vertical rupture in subducting plates and drives major along-strike change in the active margin dynamics. The causes of slab tearing in convergent settings are diverse, including (a) subduction undergoing non-uniform trench retreat velocities (Rosenbaum et al., 2008), (b) subduction accommodating trenchward slab motion with the formation of Subduction-Transform Edge Propagator faults at the surface (Govers & Wortel, 2005), (c) subduction undergoing opposing (G. Gianni et al., 2019) or differential slab rotations (Rosenbaum et al., 2019), (d) plate margin interaction with buoyant aseismic ridges (Hu & Liu, 2016), or (e) unzipping of oceanic fracture zones during subduction (Georgieva et al., 2019). Slab-tearing triggers a series of cascading effects, initially leading to the development of a vertical slab gap and toroidal flow around the slab edge with an upward component (Schellart, 2010), mantle decompression and arc-to-back arc magmatism with arc-like or asthenospheric signatures (Cocchi et al., 2017; Faccenna et al., 2007; Rosenbaum et al., 2008, 2019), an accentuated acceleration of trench retreat (Guillaume et al., 2010) and upper plate segmentation and extension/transtension (Jolivet et al., 2015; Rosenbaum et al., 2008). Hence, detecting this process in modern and ancient settings is of paramount importance to better understand recent or past changes in subduction dynamics.

While joint geophysical and geological evidence (geochemical, isotopic, structural, etc.) has proved effective for unraveling slab tears in modern settings (e.g., Faccenna et al., 2007; Rosenbaum et al., 2008, 2019), gathering similar evidence for this process in ancient and often tectonically/magmatically overprinted active margins has proved challenging. Detection of past slab-tearing events is particularly difficult for pre-Cenozoic active margins where torn slabs are now deeply subducted in the lower mantle. Recently, Gianni et al. (2019) suggested

an approach to assess this issue by combining the inspection of deep mantle domains, where a tomographically imaged slab gap in Mesozoic lower mantle slabs (van der Meer et al., 2018) was effectively linked to the tectonomagmatic record in the southwestern Pangea active margin through plate-kinematic reconstructions (i.e., tomotectonic analysis; e.g., van der Voo et al., 1999). This allowed the first recognition of an early Mesozoic slab tearing process with robust geophysical and geological records indicating a segmentation in the Early Triassic-earliest Jurassic subduction system (Charrier et al., 2007; Espinoza et al., 2019; Oliveros, Creixell, et al., 2020; Rossel et al., 2020; Vásquez et al., 2011).

Here, we study the Late Triassic-Early Jurassic magmatic record present in the Chilean Coastal Cordillera between 34° and 37°S, which allows us to better understand the dimensions and effects of the early Mesozoic slab-tearing process in southwestern Pangea. There, a series of isolated epizonal high-silica plutons intruded metamorphic rocks from the Paleozoic crystalline basement during the Late Triassic-Early Jurassic (Charrier et al., 2007; Vásquez et al., 2011). According to Vásquez et al. (2011), these rocks were emplaced in the upper crust during two pulses that occurred at ∼225–200 Ma, and ∼210–197 Ma in a retreating subduction setting during upper plate extension. The interpretation of a subduction-related process in this area is based on the documentation of a magmatic arc-like geochemical signature in the igneous rocks and the claim of coeval accretionary prism activity in the Triassic (Vásquez et al., 2011). Nevertheless, we note a strikingly high proportion of high silicic magmas (>70 wt% SiO_2) in these magmatic events, which is unexpected for subduction-related settings associated with thin upper plate crusts as those suggested in southwestern Pangea at this time (∼38 km at 210 Ma, Alasino et al., 2022). Also, some of the published geochronological controls for these rocks constraining the younger pulse of Late Triassic-Early Jurassic activity (∼210–197 Ma) are based on radiometric data that is either imprecise (Dávila et al., 1979; K-Ar data) or derived from the analysis of only few zircon grains with disparate dates (Vásquez et al., 2011), obscuring the timing of the tectonomagmatic process related to the genesis of this dominantly silicic magmatism. Therefore, additional geochemical, isotopic, and geochronological data are still needed to constrain the geodynamic setting of the Late Triassic-Early Jurassic igneous record in the Chilean Coastal Cordillera between 34° and 37°S.

In this study, we present a new set of SHRIMP U-Pb zircon age data, coupled with Lu-Hf and O isotope data for the same zircon grains and whole rock Sr-Nd-Pb isotopic and geochemical data for four Late Triassic granites between 34° and 37°S (Figure 1). This information, along with an additional tomotectonic analysis indicating a larger Late Triassic slab gap than previously acknowledged in the study area, provide key constraints to shed light on the timing, potential magmatic sources, and the geodynamic setting of the igneous activity in this key area of the southwestern margin of Pangea.

2. Tectonic Framework of the Southwestern Pangea Margin Between 34° and 37°S

In Southern Central Chile, the Carboniferous—Early Permian Gondwanide Orogeny was associated with an accretionary active margin, evidenced by remnants of an extensive subduction complex to the west, and a calc-alkaline magmatic arc to the east in the Coastal Cordillera (Hervé et al., 1988; Willner et al., 2005) (Figures 1a and 1b). The aforementioned subduction complex is composed of two voluminous parallel metamorphic units that can be traced almost uninterruptedly from 34° to 40°S (Hervé et al., 2013; Sernageomin, 2003). North of 38°S, geochronological studies carried out in these metamorphic rocks suggest some differences in the timing of deposition and provenance of the sediments, but even when the two units do not record exactly the same source patterns, it is clear that both units record a predominance of Ordovician and Mesoproterozoic sources (Hervé et al., 2013; Willner et al., 2005). The onset of subduction-related late Paleozoic magmatism in southern-central Chile has been constrained, as slightly older than ∼320 Ma (Deckart et al., 2014). This magmatic event is represented by a series of calc-alkaline tonalite, diorite, and granite plutons, with crystallization ages clustering tightly at around 295–320 Ma (Deckart et al., 2014; Hervé et al., 1988; Lucassen et al., 2004). The magmatism is characterized by a dominance of crustal recycling, likely associated with melting of the meta-sedimentary host rocks of the accretionary complex, with minor juvenile magmatic input (Deckart et al., 2014; Lucassen et al., 2004).

The transition from Gondwanide to Andean orogeny was characterized by significant changes in the tectonic configuration of the continental margin. The complete amalgamation of the Pangea supercontinent during Permian times and the related decrease in continental drift provided the kinematic and tectonic conditions for the subsequent gravitational collapse of the late Paleozoic Gondwanide Orogen (Franzese & Spalletti, 2001; Howell et al., 2005). During the Late Permian and Early Triassic, extensional reactivation of inherited Paleozoic

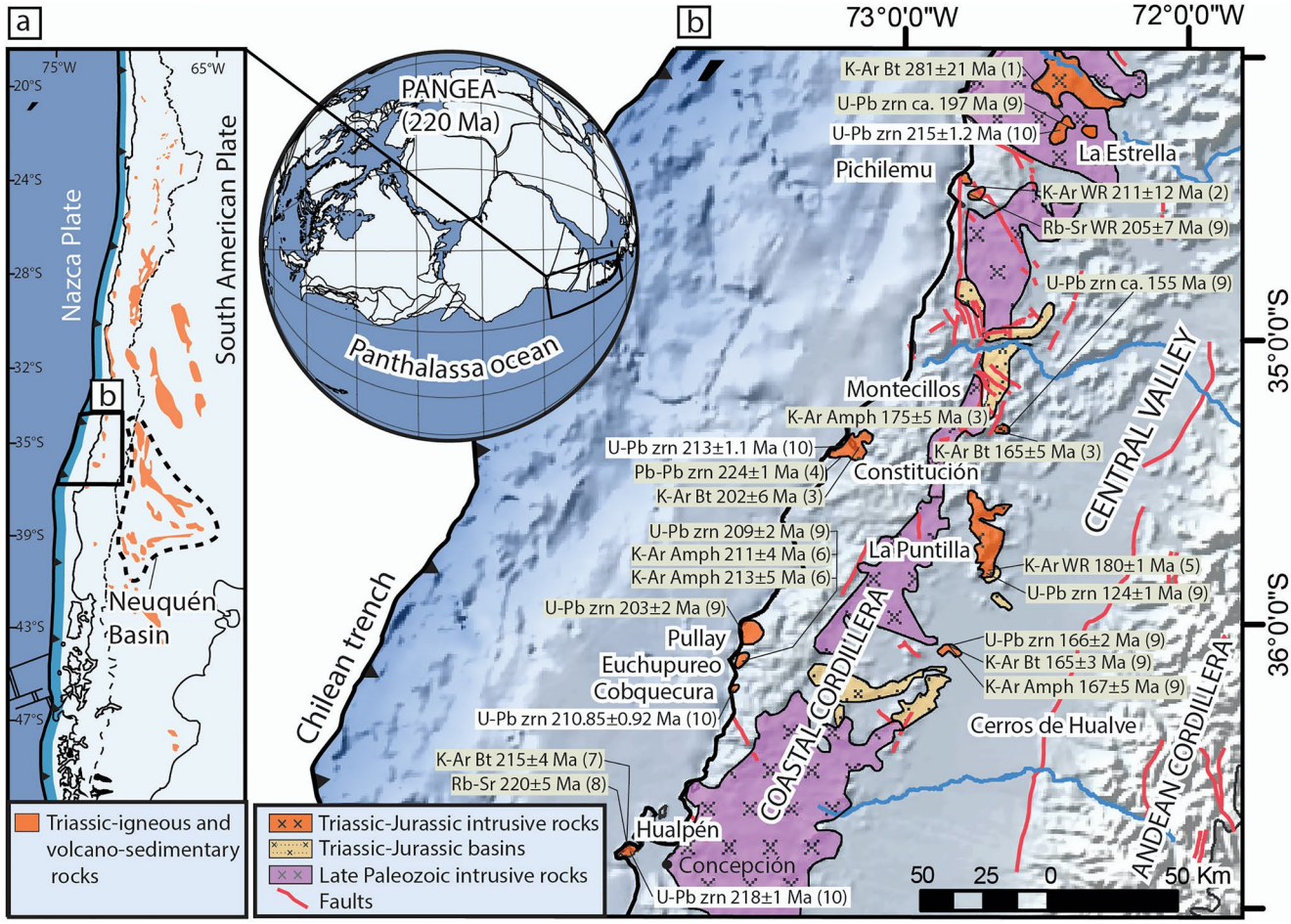

Figure 1. Outcrops of Triassic and Jurassic intrusive and sedimentary rocks in the Coastal Cordillera between 34° and 37°S. (a) Distribution of Triassic igneous and volcano-sedimentary rocks in southern South America in present day coordinates modified after Oliveros, Creixell, et al. (2020). (b) Geological sketch map of late Paleozoic to Mesozoic geological units outlined after Vásquez et al. (2011) and references therein. Plotted radiometric data from early Mesozoic Igneous rocks is from: (1) Dávila et al. (1979), (2) Hervé et al. (1984), (3) Gana and Hervé (1983), (4) Willner et al. (2005) (5), Hervé and Munizaga (1978), (6) Vásquez et al. (2005), (7) Hervé et al. (1988), (8) Lucassen et al. (2004), (9) Vásquez et al. (2011), and (10) this work. Abbreviations: Amph: amphibole; Bt: biotite; WR: whole rock; Zrn: zircon. Triassic-Jurassic basin distribution and outcrops of the Southern Coastal Batholith after Sernageomin (2003).

structures driving major crustal thinning took place in concert with extensive mesosilicic and silicic magmatic activity (e.g., del Rey et al., 2019; Franzese & Spalletti, 2001; Kay et al., 1989; Mpodozis & Kay, 1992). This tectonomagmatic stage has been recently related to the onset of a retreating subduction (del Rey et al., 2016, 2019; Oliveros, Creixell, et al., 2020) or as produced by a ~2,800 km-wide slab break-off event that triggered the extrusion of slab failure magmatism of the Choiyoi silicic large igneous province and a regional dynamic uplift along the margin of at least 1 km (G. M. Gianni & Navarrete, 2022). Voluminous magmatic activity at this time was accentuated by high upper mantle temperatures associated with Pangea supercontinent thermal insulation (Kay, 1993; Kay et al., 1989).

The Andean subduction stage is defined by a non-accretionary margin that began in Mesozoic times, with episodes of subduction erosion, particularly in the northern part of the margin segment (e.g., Rutland, 1971). The Andean subduction-related magmatism occurred in various magmatic pulses clearly distinguishable from each other, that have chemical and isotopic compositions consistent with a marked imprint of juvenile components and only a minor crustal contribution (Alasino et al., 2022; Lucassen et al., 2004; Oliveros, Creixell, et al., 2020; Oliveros, Moreno-Yaeger, & Flores, 2020; Rossel et al., 2020). The transition between Gondwanic and Andean stages is manifested in the studied area (34°–40°S) by the presence of a series of outcrops related to the so called Pre-Andean cycle (*sensu* Charrier et al., 2007), represented by small discontinuous marine to continental extensional/transtensional sedimentary basins (Hervé et al., 1976), and few isolated epizonal granitic bodies that

crop out a few kilometers immediately to the northwest of these basins (Figure 1b; Sernageomin, 2003; Vásquez et al., 2011). Concerning the plutonic activity at these latitudes, Vásquez et al. (2011) suggest that these bodies were emplaced during two pulses of activity, the first between ~225 and ~220 Ma that is associated with S and I type granites, whereas the second pulse took place between ~210 and ~197 Ma, and is linked to bimodal magmatism with some granitoids presenting anorogenic signatures. This compositional change is interpreted as resulting from a progressive shift in tectonomagmatic conditions during the transition from Gondwanide- to Andean-subduction stages. This process was characterized by a diminishing crustal influence in magma compositions as a result of the increase in fluid-induced mantle melting linked to the reactivation of the subduction and extensional conditions prevailing during this period (Charrier et al., 2007; Vásquez et al., 2011). These igneous rocks have subtle geochemical signatures consistent with subduction-related magmas from magmatic arcs (i.e., recording a Nb-Ta trough and having a positive Pb anomaly). From north to south, the granitic bodies are referred to as the La Estrella Granite, Pichilemu Granite, Constitución Granite, Cobquecura Granite, and Hualpén Stock (Figure 1).

3. Samples and Methods

In order to characterize the Late Triassic-Early Jurassic units in detail, 20 samples were collected for petrographic analysis; 10 from the La Estrella Granite, six from the Constitución granite, and four from the Hualpén Stock. Additionally, previous information regarding main characteristics of studied units is compiled and presented for comparison in Table S1 in Supporting Information S1. The foliated gabbro from southern Cobquecura was sampled and analyzed in order to complement previous isotopic data from Vásquez et al. (2011), but these gabbro samples have not been studied petrographically. For more detailed analyses of these samples, we refer the reader to Vásquez and Franz (2008) and Vásquez et al. (2009). The Pichilemu granite was not included in our study [see data from Vásquez et al. (2011)].

Thin sections were prepared by Geochronos Ltda. and studied in the optical microscopy laboratories of the Universidad Andres Bello. Sixteen samples were selected to determine whole rock major and trace compositions. Nine of these whole rock samples were selected for Sr, Nd, and Pb analysis. Four samples were selected for SHRIMP U-Pb zircon geochronology and then O and Lu-Hf isotope determinations. Exact location of analyzed samples is included in Table S2 in Supporting Information S1. Major and trace element concentrations were determined using standard XRF and ICP-MS techniques at Activation Labs in Ontario, Canada (detailed results in Table S3 in Supporting Information S1), whereas Sr-Nd and Pb isotopic work was performed in the Radiogenic Isotope Facility at the University of Arizona. For Zircon O-Hf isotopic measurements and SHRIMP Geochronology, zircon grains were separated and analyzed at the Research School of Earth Sciences (RSES/ANU), Australian National University using standard crushing, desliming, heavy liquid, and paramagnetic procedures. For more information regarding the analytical procedures see Table S4 in Supporting Information S1.

4. Results

4.1. Whole Rock Geochemistry

Main features of the analyzed samples are summarized in this section. For more detailed information see Table S3 in Supporting Information S1. Overall, the SiO_2 contents vary between 69.6% and 77.3%. Higher mean silica contents are observed in Hualpén Stock samples (74.7%), followed by La Estrella Granite (73.9%) and Constitución Granite (71.8%). Total alkalis for the studied units ranges between 9.0% and 6.7%, following the same trend as silica content with higher values in the Hualpén, followed by the La Estrella, and Constitución. Al_2O_3 contents vary between 12.3% and 14.8% with higher contents in the Constitución Granite, followed by the Hualpén Stock and La Estrella Granite. A clear negative correlation is observed between SiO_2 versus Al_2O_3, FeO_t, MgO, TiO_2, CaO, and P_2O_5 for all units. All studied rocks are subalkaline and mostly peraluminous, with the exception of the samples of the La Estrella Granite that show a metaluminous character, with low Al_2O_3 (<12.5%) and K_2O (<3.1%) in evolved and primitive samples, respectively. In terms of FeO_t and MgO contents, all samples record $FeO_t/FeO_t + MgO$ ratios between 0.97 and 0.78. A clear negative correlation is observed between SiO_2 and P_2O_5. LOI values for all the samples are below 1.1% showing a slightly inverse correlation with silica content.

Concerning minor and trace element concentrations, all measured samples show an enrichment of LILE over HFSE, Nb-Ta, Ti, Sr, and Eu, negative and positive Pb anomalies. Pronounced negative Ba and positive Cs

Table 1
Sr, Nd and Pb Isotopic Composition of Triassic Igneous Rocks in the Studied Units

Sample	$^{87}Sr/^{86}Sr_{(0)}$	$^{87}Sr/^{86}Sr_{(i)}$	2σ error	$^{143}Nd/^{144}Nd_{(0)}$	$^{143}Nd/^{144}Nd_{(i)}$	$eNd_{(0)}$	$eNd_{(i)}$	2σ error	TDM	$^{206}Pb/^{204}Pb$	$^{207}Pb/^{204}Pb$	$^{208}Pb/^{204}Pb$
EST-05	0.7832	0.7012	0.0020	0.51268	0.51249	0.8	2.5	0.0007	0.72	18.81	15.65	38.82
EST-01	0.7515	0.7075	0.0044	0.51256	0.51239	−1.5	0.5	0.0007	0.84	18.86	15.66	38.91
RAP-03	0.7341	0.7055	0.0009	0.51247	0.5123	−3.2	−1.2	0.0012	0.97	18.9	15.66	38.98
CON-06B	0.7243	0.7081	0.0017	0.5124	0.51221	−4.7	−2.8	0.0008	1.17	18.77	15.66	38.78
CON-21	0.7283	0.7082	0.0008	0.51241	0.51223	−4.4	−2.6	0.0008	1.17	18.8	15.66	38.81
CON-04	0.7267	0.709	0.0015	0.51236	0.5121	−5.5	−5.1	0.0006	3.9	18.78	15.66	38.76
CON-06A	0.7265	0.7077	0.0013	0.51243	0.51226	−4.1	−2	0.0011	1.02	18.81	15.66	38.81
HUALP-08	0.8204	0.708	0.0028	0.51249	0.51224	−3	−2.4	0.0018	2.34	19.26	15.69	38.82
HUALP 03	0.8047	0.7092	0.0014	0.51246	0.51225	−3.5	−2.2	0.0009	1.42	19.13	15.68	38.76

Note. εNd values are calculated as deviations from a chondritic uniform reservoir in part per 104, using present-day values of 143Nd/144Nd = 0.512638 and 147Sm/144Nd = 0.1967 (Faure, 1986; Wasserburg et al., 1981). 2s error for $^{206}Pb/^{204}Pb$: 0.003, $^{207}Pb/^{204}Pb$: 0.0034, and $^{208}Pb/^{204}Pb$: 0.0086. Ages of rocks are from dated samples.

anomalies are observed in the Hualpén and Constitución granites, whereas for the La Estrella granite these are incipient. A systematic decoupling between Nb and Ta is observed, probably reflecting phyllosilicate fractionation (Lynen & Cuney, 2005; Stepanov et al., 2016). REE patterns show negative slopes with flat slopes in middle and heavy REE. Higher ∑REE is observed in the La Estrella granite samples, with Yb(n) values between 11 and 60 times chondrite. Lower values are recognized in the Hualpén Stock, with Yb(n) values between 10 and 15 times the chondrite. The Eu anomalies are much more pronounced in the Hualpén Stock, whereas similar in the La Estrella and Constitución granites, but less marked in the latter unit (for more information see Supporting Information S1).

4.2. Sr-Nd and Pb Isotopes Ratios

The Sr–Nd–Pb isotope ratios of the studied samples are presented in Table 1 and are shown in Figure 2. Data were recalculated to an initial ratio at 215 Ma. The $^{87}Sr/^{86}Sr_{(i)}$ ranges between 0.7055 and 0.7092, except for sample EST-05 which has an anomalously low value of 0.7012, which is not considered in the interpretation, since it is meaningless and probably reflects analytical errors (Table 1). The Constitución and Hualpén granites samples record similar values between 0.7077 and 0.7092, whereas the La Estrella Granite has lower values of 0.7055 and 0.7075, with EST-05 even lower at 0.7012. The εNd(i) values range between 2.5 and −5.1. As with the strontium initial ratios, the Constitución and Hualpén granites record similar values of −2.0 to −5.5 and −2.4 to −2.2, respectively, although the range is very restricted (−2.0 to −2.8) if one excludes the more evolved value for sample CON-04 (at −5.5). In contrast, the La Estrella Granite samples are far less evolved, with εNd(i) values of −1.2, 0.5 and 2.5. The latter elevated value corresponds to the sample with the anomalous $^{87}Sr/^{86}Sr$(i) (EST-05). The Nd modal ages range between 0.72 and 3.90 Ga. with younger ages between 0.72 and 0.97 Ga for the La Estrella Granite and older values between 1.02 and 3.90 Ga for the Hualpén and Constitución granites.

The lead isotope ratios range from 18.77 to 19.26 for $^{206}Pb/^{204}Pb$, 15.65 to 15.68 for $^{207}Pb/^{204}Pb$ and 38.76 to 38.98 for $^{208}Pb/^{204}Pb$. Higher $^{206}Pb/^{204}Pb$ and $^{207}Pb/^{204}Pb$ values are recorded by the Hualpén Stock samples, whereas the Constitución and La Estrella granites record similar lower values relative to the Hualpén Stock. The Constitución granite has marginally lower $^{206}Pb/^{204}Pb$ ratios compared to La Estrella granites.

4.3. SHRIMP U-Pb Geochronology

Results for the four U-Pb dated granites are given in Table 2 and summarized in Figure 3. For more detailed information see Table S4 in Supporting Information S1.

4.3.1. La Estrella Granite (EST-1)

The zircons from this sample are notably equant euhedral crystals that are mainly around 100 μm in length. Many grains are cracked or are fragments of euhedral zircon. Some have central cavities consistent with rapid

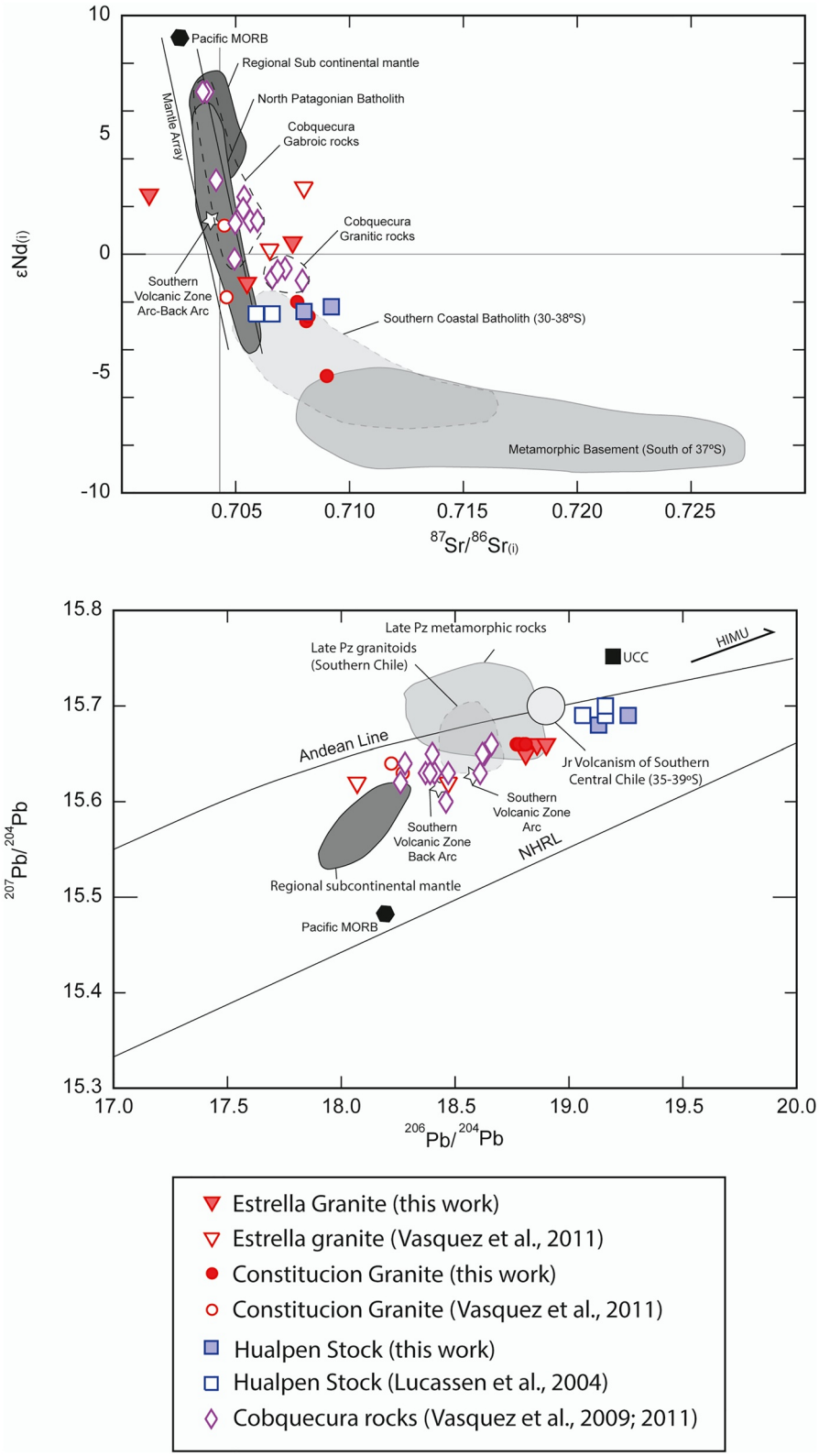

Figure 2.

crystallization at a high crustal level. The CL images show simple zoned igneous internal structures, with little evidence for older inherited components within any single grain (Figure 3). Twenty-five grains have been analyzed (Table 2, Figure 3) and three analyses are significantly enriched in common Pb (grains 6, 17, and 21), they plot well above the Tera-Wasserburg concordia and so these are not considered meaningful analyses. Three grains record Permian $^{206}Pb/^{238}U$ ages between ~275 and ~300 Ma (grains 1, 2, and 11), with another recording a middle Triassic date of ~235 Ma (grain 23). The remaining analyses form a simple bell-shaped age distribution on a probability density plot of radiogenic $^{206}Pb/^{238}U$ ages, giving a weighted mean of 215.1 ± 1.4 Ma (MSWD = 1.13 for 17 analyses). Monzogranitic sample EST-1 from La Estrella Granite yielded a mean crystallization age of 215 ± 1.2 Ma on the base of 17 concordant zircons. This is interpreted as the time of zoned igneous zircon crystallization.

4.3.2. Constitución Granite (CON-23)

The zircons from this sample are elongate euhedral crystals, some are prismatic, and others have a pyramidal termination. The grains are around 100–250 μm in length and some have worm-like central cavities commonly seen in high level to subvolcanic igneous rocks. Inclusions of apatite are also notable. The CL images show mainly length parallel zoning, with some oscillatory zoned grains (Figure 3). Twenty-five areas have been analyzed on 22 zircon grains (Table 2, Figure 3). The two analyzes of grain 13 record anomalous older Ordovician $^{206}Pb/^{238}U$ ages of ~455–470 Ma and this grain is either a contaminant or an extraneous inherited older component; it does not have a younger Triassic rim and so there is no clear evidence for it being an inherited zircon grain. Analysis of grain 5, and the central area to grain 18, record middle Triassic $^{206}Pb/^{238}U$ ages of ~235 and 225 Ma, respectively. Importantly, analysis of the zoned outer area to grain 18 records a $^{206}Pb/^{238}U$ age that is within uncertainty of the majority of the other zoned igneous areas analyzed, around 215 Ma. This provides clear evidence for slightly older inherited zircon components within the population. An enlarged probability density plot of radiogenic $^{206}Pb/^{238}U$ ages shows a dominant age peak (Figure 3), with a slight skew to the younger age side. There is clear evidence for radiogenic Pb loss with the younger date recorded by grain 16. A weighted mean $^{206}Pb/^{238}U$ age for the dominant age grouping is 213.2 ± 1.3 Ma (MSWD = 1.06 for 19 analyses) and this constrains the time of igneous zircon crystallization.

4.3.3. Cobquecura Granite (COB-GB)

The zircons from this gabbroic sample are elongate euhedral crystals, some with bipyramidal terminations, others prismatic or fractured parts of such grains. The grains range to at least 350 μm in length with many ≥150 μm. Whilst some grains are clear under transmitted light, a few have elongate central cavities consistent with rapid crystallization. Twenty-two zircons have been analyzed (Table 2, Figure 3). All 22 areas analyzed yield concordant data as can be seen on the Tera-Wasserburg plot and form a simple bell shaped distribution of radiogenic $^{206}Pb/^{238}U$ ages (Figure 3). A weighted mean for all 22 analyses has no excess scatter (MSWD = 0.66) giving a $^{206}Pb/^{238}U$ age of 210.9 ± 1.3 Ma constraining the time of igneous zircon crystallization.

4.3.4. Hualpén Stock (HUALP-04)

The zircons from this sample are elongate euhedral crystals, mainly prismatic in shape, but a few have a pyramidal termination. The grains range to at least 300 μm in length; many are ≥100 μm. Under transmitted light, central cavities are prominent indicating rapid crystallization at a high crustal level. The CL images show predominantly length parallel zoning, with some oscillatory zoned areas (Figure 3). Twenty-six areas have been analyzed on 25 zircon grains have been analyzed; although the analysis of grain 17 was not completed (Table 2, Figure 3). The area analyzed on grain 16 is significantly enriched in common Pb and has likely lost significant amounts of radiogenic Pb; it is not considered further. The majorities of the other areas analyzed are dominated by radiogenic Pb and form a prominent cluster, close to, or within uncertainty of the Tera-Wasserburg concordia (Figure 3). The analysis of grain 9 has younger $^{206}Pb/^{238}U$ age and it is likely that the area analyzed has also lost some radiogenic Pb. Analyses of grains 13 and the central area to grain 21 record slightly older $^{206}Pb/^{238}U$ ages of ~230 and ~235 Ma, respectively. Analysis of the zoned tip to grain 21 records a $^{206}Pb/^{238}U$ age that is within uncertainty of

Figure 2. Above is a diagram of $^{87}Sr/^{86}Sr$ versus εNd initial values from Upper Triassic Granites cropping out in Coastal Cordillera between 34° and 37°S. BSE: Bulk Silicate Earth. Ages corrected for in situ decay at 220 Ma. MORB is actually MORB corrected for in-situ decay considering 220 Ma. Below is a diagram of $^{207}Pb/^{204}Pb$ versus $^{206}Pb/^{204}Pb$ initial isotopic ratios for Upper Triassic Granites cropping out in Coastal Cordillera between 34° and 37°S. Regional Sub Continental Mantle, North Patagonian Batholith, Southern Coastal Batholith and Metamorphic basement fields after Lucassen et al. (2004). Active Southern Volcanic Zone Arc and Back Arc after Jacques et al. (2013).

Table 2
Summary of Oxygen and Lu-Hf Isotope Data for Zircon Spot Analyses

Analysis spot ID	Spot age (Ma)	±	$^{18}O/^{16}O$	±(10^{-7})	$d^{18}O$ ‰	±2σ	$^{176}Yb/^{177}Hf$	$^{176}Lu/^{177}Hf$	$^{176}Hf/^{177}Hf$	±(10^{-6})	e Hf (0)	eHf (i)	±2σ	t_{DM2} (Ga)
EST-1														
1.1	279.1	3.6	0.0020456	2	5.165	0.36	0.05590	0.001788	0.282657	41	−4.53	1.35	1.45	1.13
2.1	299.4	3.7	0.0020462	2	5.459	0.36	0.03300	0.001134	0.282538	43	−8.73	−2.30	1.52	1.38
3.1	216.1	2.5	0.0020446	2	4.646	0.37	0.05310	0.001685	0.282729	42	−1.98	2.58	1.49	1.00
4.1	218.8	2.9	0.0020443	2	4.508	0.35	0.03181	0.001014	0.282725	29	−2.12	2.60	1.03	1.00
5.1	210.4	2.3	0.0020429	2	3.838	0.33	0.08250	0.002465	0.282694	79	−3.22	1.12	2.79	1.09
6.1	197.2	2.4	0.0020442	2	4.446	0.37	0.06870	0.002170	0.282731	59	−1.91	2.19	2.09	1.01
7.1	212.9	2.4	0.0020435	2	4.122	0.34	0.07030	0.002336	0.282706	51	−2.79	1.61	1.80	1.06
8.1	213.6	3.1	0.0020439	2	4.322	0.36	0.04650	0.001503	0.282730	38	−1.94	2.59	1.34	1.00
9.1	222.3	2.6	0.0020432	3	3.988	0.39	0.06800	0.002172	0.282742	39	−1.52	3.10	1.38	0.97
10.1	208.4	2.3	0.0020441	2	4.404	0.34	0.07850	0.002580	0.282761	47	−0.85	3.43	1.66	0.94
11.1	273.4	4.0	0.0020475	2	6.075	0.36	0.05200	0.001827	0.282589	37	−6.93	−1.18	1.31	1.28
12.1	212.1	2.5	0.0020452	2	4.980	0.37	0.09150	0.002960	0.282744	52	−1.45	2.85	1.84	0.98
13.1	214.9	2.9	0.0020443	3	4.508	0.39	0.05190	0.001840	0.282725	85	−2.12	2.40	3.01	1.01
14.1	212.8	2.4	0.0020431	3	3.913	0.44	0.06580	0.002080	0.282707	68	−2.76	1.68	2.41	1.06
15.1	208.5	2.4	0.0020421	2	3.442	0.37	0.06420	0.002050	0.282690	74	−3.36	0.99	2.62	1.10
16.1	214.6	2.3	0.0020440	2	4.378	0.38	0.11900	0.003460	0.282763	100	−0.78	3.50	3.54	0.94
17.1	217.2	3.4	0.0020446	2	4.671	0.37	0.04150	0.001340	0.282741	35	−1.56	3.08	1.24	0.97
18.1	214.1	2.8	0.0020437	3	4.236	0.40	0.03502	0.001146	0.282661	68	−4.38	0.21	2.41	1.15
CON-23														
1.1	211.6	2.5	0.0020515	2	8.059	0.36	0.05600	0.001940	0.282716	51	−2.44	1.99	1.80	1.03
2.1	213.7	2.5	0.0020520	2	8.265	0.37	0.03390	0.001095	0.282766	44	−0.67	3.92	1.56	0.91
3.1	215.6	2.3	0.0020520	2	8.258	0.38	0.11240	0.003540	0.282720	64	−2.30	1.99	2.26	1.04
4.1	216.3	2.5	0.0020513	2	7.952	0.38	0.08780	0.002760	0.282763	46	−0.78	3.64	1.63	0.93
5.1	235.3	2.9	0.0020506	3	7.600	0.42	0.05940	0.001950	0.282748	64	−1.31	3.62	2.26	0.95
6.1	207.4	2.7	0.0020530	3	8.753	0.39	0.03120	0.001120	0.282684	50	−3.57	0.89	1.77	1.10
7.1	213.3	3.5	0.0020508	2	7.685	0.35	0.01921	0.000676	0.282718	61	−2.37	2.28	2.16	1.02
8.1	208.7	2.3	0.0020522	2	8.368	0.38	0.05780	0.001846	0.282735	37	−1.77	2.62	1.31	0.99
9.1	205.5	2.4	0.0020518	2	8.164	0.37	0.06490	0.002000	0.282770	45	−0.53	3.77	1.59	0.92
10.1	215.7	2.9	0.0020511	2	7.863	0.38	0.03550	0.001143	0.282708	54	−2.72	1.91	1.91	1.04
11.1	209.8	2.2	0.0020524	3	8.485	0.39								
12.1	214.5	2.4	0.0020517	2	8.111	0.38								
13.1	468.2	5.1	0.0020512	2	7.904	0.37	0.05270	0.001870	0.282341	47	−15.70	−5.86	1.66	1.73
14.1	212.2	2.4	0.0020527	3	8.613	0.40	0.04960	0.001470	0.282742	89	−1.52	2.99	3.15	0.97
15.1	212.3	3.3	0.0020532	2	8.846	0.37	0.04070	0.001320	0.282606	93	−6.33	−1.80	3.29	1.28
16.1	199.5	2.3	0.0020507	2	7.666	0.38	0.05440	0.001817	0.282707	46	−2.76	1.44	1.63	1.06
17.1	214.4	2.6	0.0020511	2	7.863	0.37	0.05250	0.001776	0.282746	55	−1.38	3.14	1.95	0.96
18.1	223.3	2.5	0.0020527	2	8.617	0.37								
COB-GB														
1.1	209.7	2.2	0.0020424	4	6.278	0.51	0.24820	0.006219	0.282974	65	6.68	10.49	2.30	0.49
2.1	210.8	2.2	0.0020424	2	6.304	0.37	0.22970	0.005653	0.282912	57	4.49	8.39	2.02	0.63
3.1	212.9	2.2	0.0020425	3	6.330	0.39	0.22390	0.005821	0.282931	49	5.16	9.08	1.73	0.58

Table 2
Continued

Analysis spot ID	Spot age (Ma)	±	$^{18}O/^{16}O$	±(10^{-7})	$d^{18}O$ ‰	±2σ	$^{176}Yb/^{177}Hf$	$^{176}Lu/^{177}Hf$	$^{176}Hf/^{177}Hf$	±(10^{-6})	e Hf (0)	eHf (i)	±2σ	t_{DM2} (Ga)
6.1	210.9	3.2	0.0020418	5	6.022	0.57	0.23730	0.005970	0.282936	53	5.34	9.20	1.88	0.58
7.1	213.9	2.2	0.0020421	2	6.159	0.35	0.26119	0.006708	0.283006	48	7.81	11.63	1.70	0.42
8.1	209.4	2.1	0.0020426	3	6.376	0.41	0.23760	0.005867	0.282955	53	6.01	9.86	1.88	0.53
10.1	209.3	2.2	0.0020422	3	6.188	0.41	0.19850	0.005086	0.282908	49	4.35	8.30	1.73	0.63
11.1	211.9	2.2	0.0020425	5	6.340	0.57	0.29460	0.007500	0.282952	63	5.90	9.57	2.23	0.55
12.1	211.0	2.2	0.0020423	3	6.265	0.38	0.18560	0.004703	0.282913	51	4.53	8.56	1.80	0.62
13.1	209.5	2.2	0.0020426	3	6.379	0.40	0.24110	0.006225	0.282964	53	6.33	10.13	1.88	0.52
15.1	210.7	2.2	0.0020421	2	6.146	0.37	0.22440	0.005602	0.282929	50	5.09	9.00	1.77	0.59
16.1	209.8	2.2	0.0020425	3	6.336	0.44	0.20370	0.005240	0.282917	50	4.67	8.61	1.77	0.61
17.1	211.2	2.2	0.0020421	2	6.156	0.37	0.24740	0.006237	0.282975	50	6.72	10.55	1.77	0.49
19.1	210.8	2.2	0.0020435	3	6.849	0.43	0.20480	0.005249	0.282922	55	4.84	8.80	1.95	0.60
20.1	213.7	2.2	0.0020425	3	6.348	0.40	0.17600	0.004508	0.282864	39	2.79	6.91	1.38	0.72
22.1	210.6	2.2	0.0020435	4	6.857	0.52	0.28300	0.006978	0.282944	55	5.62	9.33	1.95	0.57
HUALP-04														
1.1	218.5	2.6	0.0020501	2	7.345	0.38	0.09830	0.003440	0.282689	45	−3.39	0.97	1.59	1.11
2.1	218.3	2.4	0.0020511	3	7.825	0.39								
3.1	219.9	2.3	0.0020526	2	8.566	0.37	0.07140	0.002450	0.282712	53	−2.58	1.95	1.88	1.04
4.1	219.7	2.5	0.0020500	2	7.279	0.35								
5.1	218.8	2.4	0.0020495	3	7.051	0.40								
6.1	220.6	2.3	0.0020516	2	8.074	0.36								
7.1	218.0	2.3	0.0020519	2	8.211	0.34								
8.1	216.5	2.3	0.0020521	2	8.351	0.38	0.12170	0.004035	0.282743	52	−1.49	2.75	1.84	0.99
9.1	210.4	2.2	0.0020526	2	8.552	0.36								
10.1	219.0	2.4	0.0020505	2	7.546	0.35								
11.1	215.1	2.3	0.0020515	2	8.017	0.36								
12.1	215.6	2.3	0.0020526	2	8.598	0.38	0.09920	0.003200	0.282713	73	−2.55	1.79	2.58	1.05
13.1	229.0	2.6	0.0020496	3	7.126	0.40								
14.1	220.3	2.3	0.0020524	2	8.494	0.37								
15.1	217.7	2.5	0.0020502	3	7.400	0.39	0.08240	0.002847	0.282729	72	−1.98	2.45	2.55	1.01
16.1	172.2	2.3	0.0020514	2	7.992	0.36								
17.1	*218.8*	*1.2*	0.0020538	2	9.153	0.33								
18.1	220.7	2.4	0.0020517	3	8.124	0.45	0.03980	0.001346	0.282757	49	−0.99	3.72	1.73	0.93

Note. Oxygen isotope ratios normalized relative to FC1 = 5.61‰. ^{176}Lu decay constant of 1.865×10^{-11} (Soderlund et al., 2004). $^{176}Hf/^{177}Hf$ and $^{176}Lu/^{177}Hf$ of CHUR values of 0.282785 and 0.0336 (Bouvier et al., 2008). Present day depleted mantle values of $^{176}Hf/^{177}Hf$ and $^{176}Lu/^{177}Hf$ of 0.283225 and 0.0385 (Vervoort & Blichert-Toft, 1999) and the bulk earth $^{176}Lu/^{177}Hf$ value of 0.015 (Goodge & Vervoort, 2006). Italic values are the name of each analized sample.

the main grouping and this provides clear evidence for the presence of slightly older middle Triassic inheritance. A weighted mean for the remaining 21 analyses has no excess scatter (MSWD = 0.80) giving a $^{206}Pb/^{238}U$ age of 218.8 ± 1.2 Ma and thereby constraining the time of igneous zircon crystallization.

4.4. O and Lu-Hf Isotope Data

The O and Lu-Hf isotopic data is presented in Table 2 and summarized in Figure 4. Measured $\delta^{18}O$ values range from 3.2‰ to 9.2‰ with values at the lower end below those recorded by mantle zircons and those at the upper

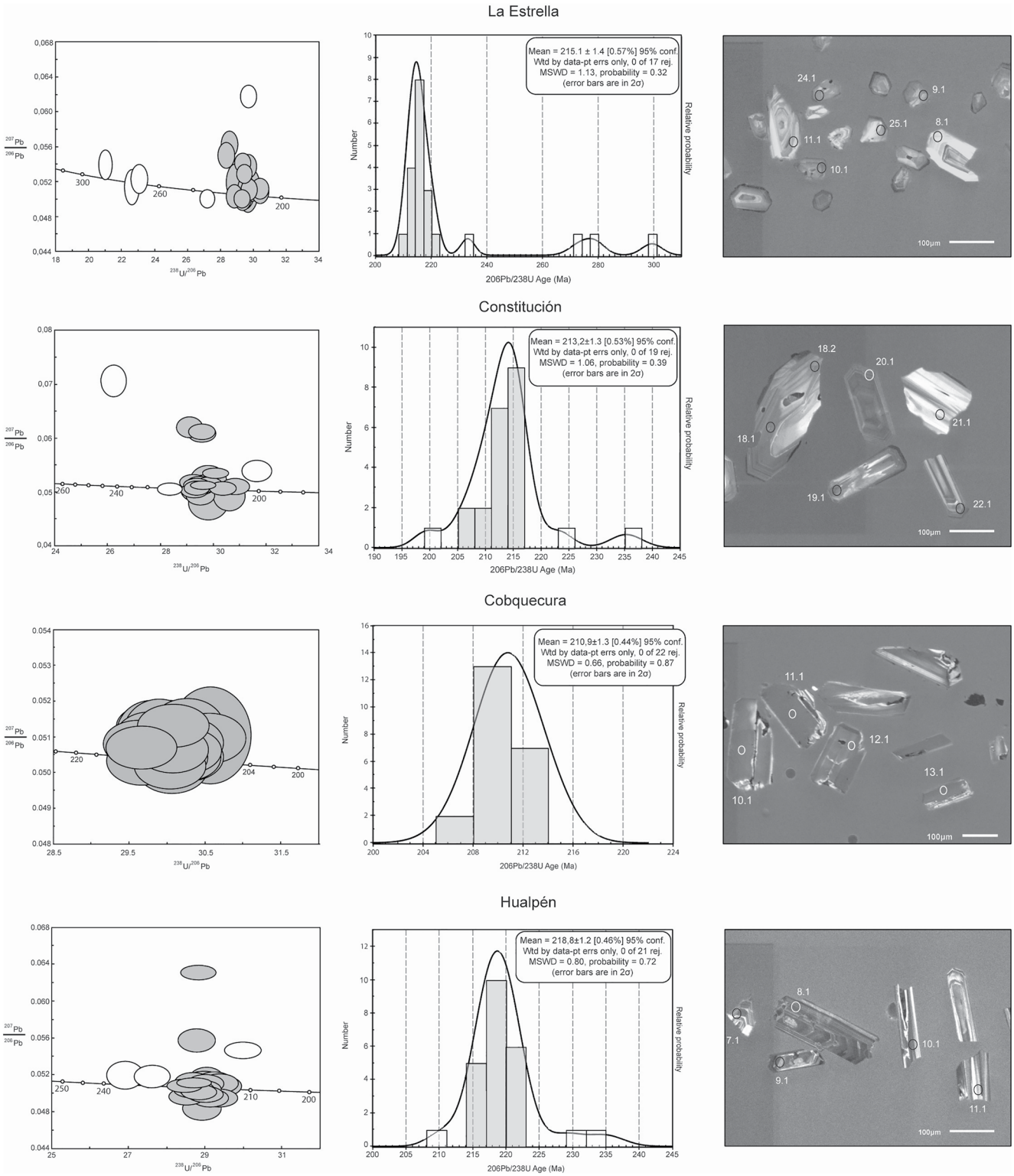

Figure 3. Obtained SHRIMP U\Pb geochronological data from studied Upper Triassic Granites in the Chilean Coastal cordillera between 34° and 37°S.

end with values indicative of magmatic zircon derived from sedimentary source(s) (Table 2). In detail, the La Estrella Granite values range from 3.4‰ to 6.1‰, with most values between ~3.9‰ and ~5.5‰; the median value is 4.4‰. The Constitución and Hualpén samples record higher $\delta^{18}O$ values between 7.1‰ and 9.2‰ with median values of 8.14‰ and 8.05‰, respectively. In contrast, the Cobquecura gabbro records a notably restricted

10.1029/2022TC007354

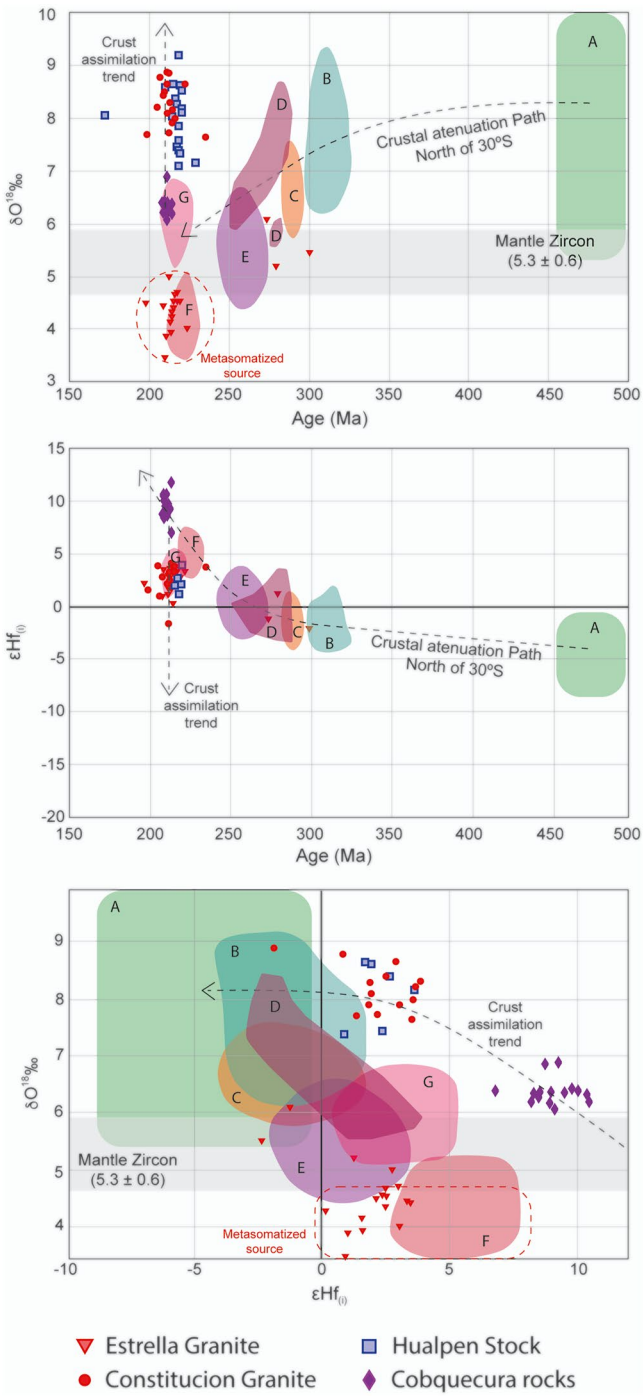

Figure 4. Age (Ma) verssus (a) $\delta^{18}O$ and (b) $\varepsilon Hf_{(i)}$ diagram. (c) Initial εHf versus $\delta^{18}O$ diagram. Fields after (a) Famatinan Magmatism of Sierras Pampeanas (Rapela et al., 2018). (b) Coastal Batholith (Deckart et al., 2014). (c) Permian Frontal Andes Batholith (Hervé et al., 2014). (d) Frontal Cordillera and Precordillera in Argentina (Poole et al., 2020). (e) Frontal Andes Batholith (Del Rey et al., 2016). (f and g) Triassic Frontal Andes Batholith (Hervé et al., 2014).

range of intermediate $\delta^{18}O$ values, between 6.0‰ and 6.9‰, with a median value of 6.3‰. This is just above that recorded by mantle zircons.

Overall, the calculated initial εHf(i) values also show a broad range from −2.3 to +11.6 (Table 2, Figure 4). Unfortunately, not all the zircon grains analyzed for O isotopes were able to withstand the rigors of the laser Hf analyses. This is particularly the case for the Hualpén zircon grains with only 6 completed analyses. Those record a relatively restricted range from around +1.0 to +3.7 (Table 2). The La Estrella and Constitución samples also record similar, relatively narrow ranges of initial Hf ratios between −2.3 and + 2.5, and −1.8 and + 3.9, respectively. Zircons from the Cobquecura gabbro have more radiogenic initial Hf ratios, ranging from +6.9 to +11.6, although most are between +8.3 and +10.6 (Table 2). Contemporary depleted mantle would be around +14.9.

5. Discussion

5.1. Geochronological Constraints on Late Triassic Magmatism in South-Central Chile

The new geochemical, isotopic, and geochronological data from Upper Triassic granitoids of the Coastal Cordillera of Central Chile (34°–37°S) allow further insights into their timing and origin. Concerning the previous geochronological constraints in these rocks, Vásquez et al. (2011), suggested two distinct pulses of igneous activity. The first, associated with the intrusion of S to S/I-type granites of the Pichilemu, Constitución, and Hualpén granitoids, between ~225 and 220 Ma, whereas the second pulse was related to the intrusion of A-Type granites of the La Estrella and Cobquecura granitoids, between ~210 and 197 Ma. According to Vásquez et al. (2011), the origin of the Late Triassic magmatism is related to a retreating subduction regime involving oblique subduction, with a ~210–197-Ma episode of slab steepening, in which successive changes in composition were related to the progressive thinning of the upper-plate. Nevertheless, as mentioned before, the geochronological data used to constrain the younger magmatic pulse is rather unreliable. The new ages presented here indicate that the Late Triassic magmatic activity occurred in a single, relatively short-lived event, ranging from approximately 220 to 210 Ma, which is consistent with most of the geochronological data available in the area (Figure 5).

Sixteen of the 19 available ages overlap within the analytical uncertainty of this age range. These updated geochronological constraints require a reconsideration of the current tectonomagmatic model since a wide spectrum of compositions should be generated in a rather short areal and temporal window. Although most of the measured grains reflect a consistent and concordant crystallization age for all the studied units, there is a small but consistent presence of slightly older zircons with ages ranging between 220 and 235 Ma in high-silica samples. This is consistent with main crystallization ages recognized in some granitic bodies of northern Chile (Coloma et al., 2017; Hervé et al., 2014; Maksaev et al., 2014; Mpodozis & Kay, 1992), and could reflect that early stages of rifting and magmatism observed in northern Chile (Ramos & Kay, 1991) also took place at these latitudes, and that related early igneous rocks were partially assimilated by the younger pulse at 210–220 Ma.

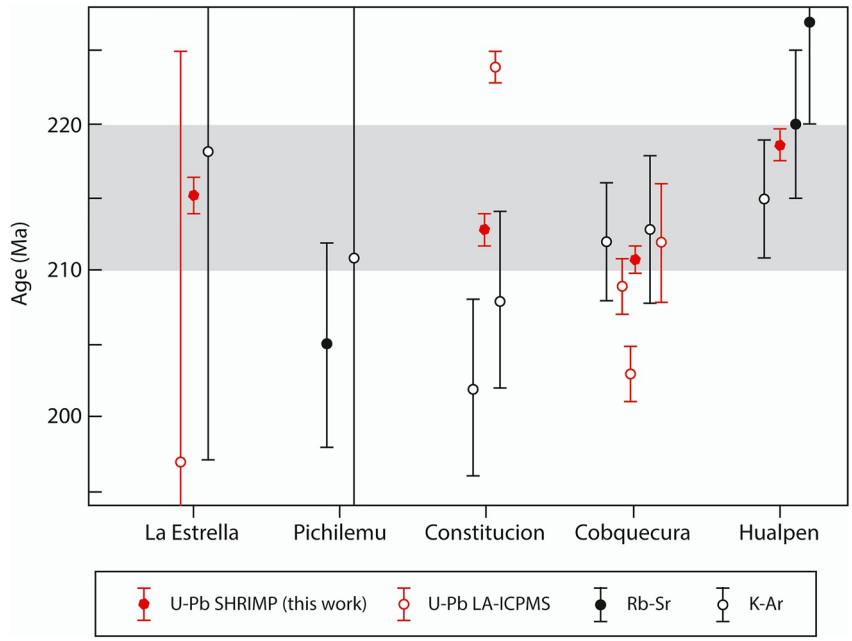

Figure 5. Compiled Geochronology for Upper Triassic granites in the studied area. Gray area between 220 and 210 Ma shows that most of the data overlaps in this time span. References in the main text.

5.2. Petrogenesis of the Late Triassic Granitoids on South-Central Chile

Vásquez et al. (2011) interpreted a subduction-related origin for the Late Triassic granitoids based on two arguable lines of evidence. First, they recognized a subduction-related signature in these rocks as documented by a Nb-Ta trough and a positive Pb anomaly. Second, these authors favored an ongoing subduction process in the Late Triassic by claiming the existence of an active accretionary prism at this time. Nevertheless, subduction-related geochemical signatures could also be entirely inherited (e.g., Richards, 2009), especially considering the high amount of highly evolved rocks in the area. This could be expected for rocks produced by melting metasomatized sublithospheric mantle or continental crust (e.g., van Hinsbergen et al., 2020 and references therein). Most importantly, at present, there is no evidence of an Upper Triassic accretionary complex in this sector of the plate margin as suggested by Vásquez et al. (2011) to support ongoing subduction beneath the study area coeval to the magmatic activity. Indeed, as the Late Triassic magmatism intruded the late Paleozoic accretionary prism, it was considered by Willner et al. (2005) as the geological manifestation of the ending of the accretionary process at these latitudes. Therefore, an origin related to a typical subduction system for the Late Triassic-Early Jurassic granitoids in the study area is at least questionable.

One of the most striking features of the Late Triassic magmatism of Southern Central Chile is the marked dominance of highly evolved rocks generated under extensional conditions (e.g., Charrier, 1979; Vásquez et al., 2011), which is not only observed for the granitic units studied here, but also for volcanic counterparts recognized in spatially related sedimentary basins (Figure 1b; Hervé et al., 1976). This high proportion of rhyolitic/granitic compositions contrasts the results presented by Oliveros, Creixell, et al. (2020) in northern Chile, where a significant volume of intermediate to mafic rocks has been documented, consistent with a typical subduction-related environment.

The contrasting nature of contemporaneous igneous units along the Western Margin of Pangea is still not completely understood. As argued in the following subsections, we suggest that the change in magma composition likely indicates the existence of a north-south segmentation in the early Mesozoic process of magmagenesis. Moreover, the dominance of εNd values in the proximities of contemporaneous CHUR compositions, lead isotopic values systematically more enriched than subcontinental mantle values in almost all studied units (Figure 2), and consistent Mesoproterozoic Nd and Hf modal ages suggest a significant participation of an anatectic process (Guo et al., 2021; Zhao et al., 2021) in the formation of the Upper Triassic units cropping out between 34° and 37°S. However, given the dominance of positive εHf(i) values and the non-highly radiogenic Sr and Nd

isotopic compositions of the majority of the studied samples (Figure 2) it is clear also that mantle melting was an important counterpart in the genesis of the granites as crustal melts tend to show more enriched isotopic signatures (Antunes et al., 2008; Appleby et al., 2010; Siebel & Chen, 2009).

5.2.1. Peraluminous Granites of Constitución and Hualpén

These units are characterized by high elemental Cs (10–24 ppm) and Pb (25–37 ppm) concentrations and highly enriched Sr, Nd, and Pb isotopic ratios, especially in samples from the Hualpén granite. The close to CHUR εHf(i) values and O isotopic ratios systematically over seven in measured zircons of these units suggest a major involvement of continental crust in the genesis of the magmas (Figure 4). These are common features for S-type granites that usually result from melting metapelitic sediments at middle/lower crustal levels (Chappell & White, 1974; Zhu et al., 2020). Also, this is consistent with the geological relation of the peraluminous granites, intruding the metapelitic rocks of the Paired Metamorphic Belt of Southern Central Chile (Hervé et al., 1988, 2013), and with the presence of few pelitic xenoliths recognized in rocks of Hualpen Stock (Figure S1f in Supporting Information S1).

Discrimination diagrams show that the Hualpén and Constitución granites plot in the S- and S/I- Type granites field, respectively, and define a trend in the syn-collisional granites field, which is more evident in the Hualpén igneous rocks (Figures 6a–6c). The Pb versus Ba diagram of Finger and Schiller (2012) indicates affinities with hot granites for these rocks, implying partial melting of a pelitic assemblage composed by Bt + Sil + Qz + Pg or Bt + Qz + Pl (Le Breton & Thompson, 1988; Vielzeuf & Holloway, 1988; Vielzeuf & Montel, 1994) (Figure 6d). Considering the observed mineralogical features of the metamorphic basement in the study area (Willner et al., 2005), the former is the most likely source. Cold granites usually do not segregate from the source area given the small amount of partial melting induced at low temperatures; if they do so, tectonic squeezing is needed to facilitate their ascent to higher crustal levels (Finger & Schiller, 2012). The latter is not compatible with geological observations in the study area, considering the dominantly extensional conditions prevailing in the crust during the Late Triassic in southwestern Pangea.

Considering the above, the total area of exposure of Constitucion granite, the presence of local mingling with less evolved magmas, it is possible to infer that peraluminous granites of Constitucion are the result of 20%–40% of partial melting of a metapelitic biotite bearing middle/lower crust (Clemens & Vielzeuf, 1987; Stevens et al., 1997). This anatectic process could be induced, and compositionally influenced, by mafic magmas underplated at the base of the crust (Zhou et al., 2021) as a result of adiabatic melting of the asthenospheric mantle in response to generalized extensional conditions that rule the margin during the Late Triassic (Charrier et al., 2007). This scenario explains the "hot nature" of Constitución granite, the Sr and Nd isotopic signature of some samples in an intermediate position between the Paleozoic Basement and the sub-lithospheric mantle and the systematically positive $\varepsilon Hf_{(i)}$ values of the samples of these units (Figure 2). In this context, the leucocratic granites of Hualpén would represent a less mantle-influenced portion of the anatectic melts since they show higher isotopic lead enrichment (Figure 2). These magmas probably reached higher crustal levels, as suggested by zircon morphologies (Figure 3) and field observations that indicate a higher proportion of miarolitic cavities in the Hualpén stock (Figure S1 in Supporting Information S1).

5.2.2. The Cobquecura Gabbros

Bimodal magmatism of Cobquecura area was interpreted by Vásquez et al. (2009) as a mixture of MORB-like melted subcontinental mantle and Paleozoic middle continental crust on the basis of geochemical and Sr-Nd and Pb whole rock isotopic data. According to these authors, this hybrid magma resulted from the assimilation of a thinned continental crust by partial melts generated during slab retreat and subsequent asthenospheric upwelling. Concerning the genesis of Gabbroic rocks from the Cobquecura area, Vásquez et al. (2009) indicate arc affinities for the mafic magmas and isotopic similarities between subcontinental mantle and less evolved gabbronoritic samples and a crustal contribution was observed in the slightly evolved gabbroic rocks. The Sr, Nd, Pb, O, and Hf isotopic data presented here agrees with these findings and confirms the existence of a slight crustal influence for the gabbroic portion (Figures 2 and 4), suggesting that crustal signatures in this portion of the magmatic suite were possibly related to early assimilation events in the hot zone (*sensu* Annen et al., 2006).

5.2.3. La Estrella Granite

High-alkali and silica contents, CHUR-like Sr and Nd isotope ratios, and especially, low $\delta^{18}O$ isotopic values (lower than the mantle zircon isotopic composition, Valley et al., 2005) suggest that these granitic magmas are

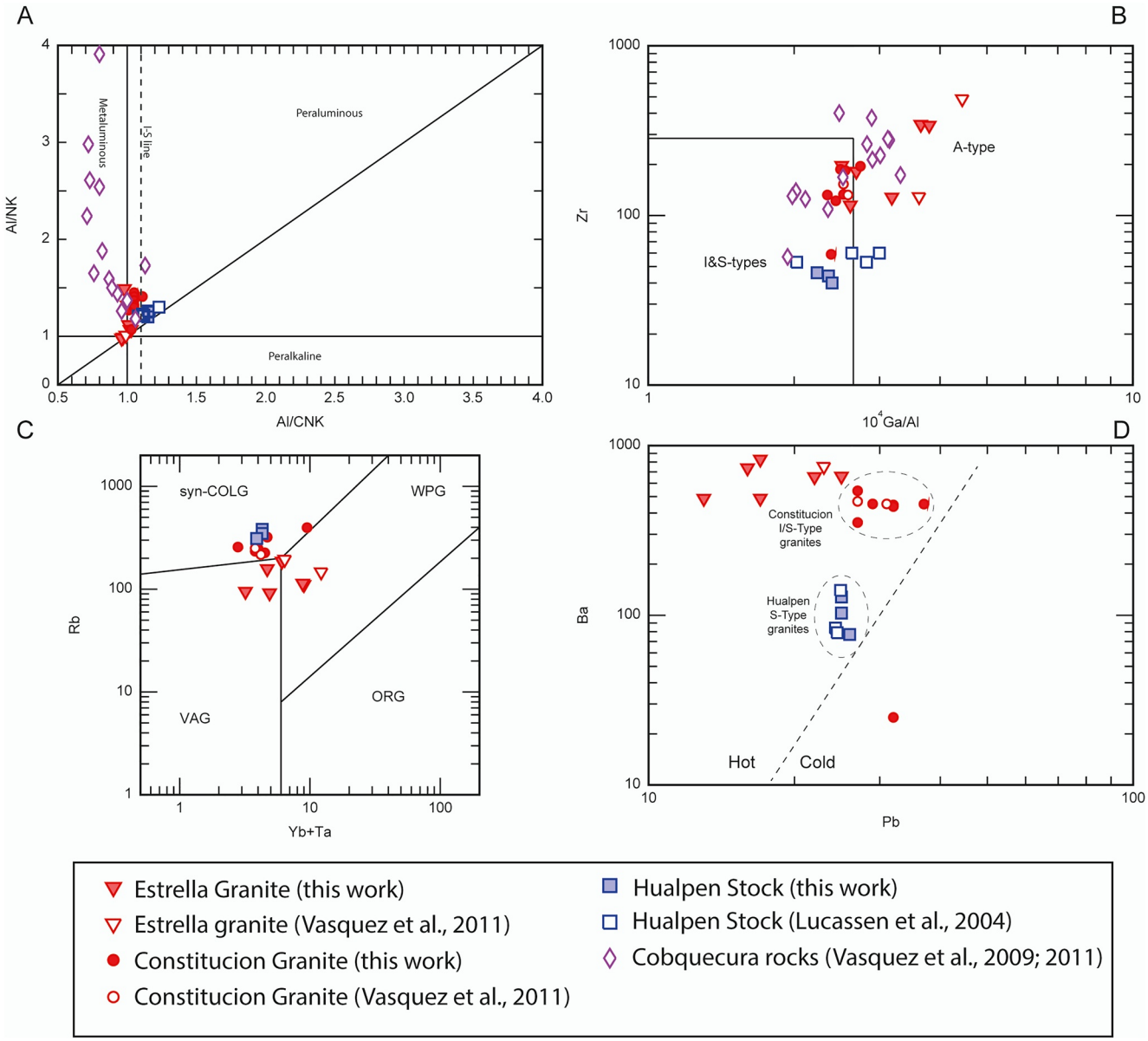

Figure 6. Discriminant diagrams for studied samples. (a) Al/CNK versus Al/NK (Shand, 1947). (b) Ga/Al versus Zr (Whalen et al., 1987). (c) Ta + Yb versus Rb (Pearce et al., 1984). (d) Pb versus Ba (Finger & Schiller, 2012).

not typical anatectic products derived from melting of a granulitic continental lower crust (Collins et al., 1982). According to Vásquez et al. (2006, 2011), these rocks reflect reducing conditions related to an anorogenic environment. However, they do not specify the associated petrogenetic process responsible for the genesis of these magmas. Reducing and dominantly anhydrous conditions in contrast to the other units studied in this work could reflect differences in the source of the magmas. This is consistent with the inland position of La Estrella granite and the emplacement in Paleozoic granitic rocks (Figure 1b). Contrary to peraluminous rocks of Constitución and Hualpen, these rocks probably do not result from melting of pelitic sources but from former granitic arc basements, likely melted and mixed with underplated asthenospheric basaltic magmas resulting from rifting conditions in the area. Troch et al. (2020) indicate that low $\delta^{18}O$ values in highly silicic rocks are commonly related to rifting events, where the upper to middle crust is hydrothermally altered at high temperatures (350°C–400°C) and subsequently melted by subsequent magmatic pulses (Guo et al., 2019; Troch et al., 2020). Thus, mineralogical, chemical, and isotopic characteristics of the La Estrella Granite, point to an anorogenic rift-related setting linked to the prolonged extensional conditions that prevailed in the southwestern Pangea margin since the mid-Permian

(Ramos & Kay, 1991). The presence of discrete populations of Permian and Late Triassic zircon grains in sample EST-1 (Figure 3) is consistent with this hypothesis, suggesting that older frozen pulses of magmatism were continuously influenced, hydrothermally altered, and partially recycled during this and previous rifting episodes that are best recognized in northern areas of the margin (Mpodozis & Kay, 1992).

5.3. A New Tectonomagmatic Model and Tectonic Implications for the Late Triassic in South-Central Chile

As mentioned above, petrogenetic conditions associated with the Late Triassic Granites of Central Chile indicate a mixture of crustal and asthenospheric melts. Considering the high dominance of subduction-derived rocks in pre-Andean basement (e.g., Deckart et al., 2014), the possibility of geochemical inheritance of arc-like signatures in the Late Triassic granites should be seriously considered. Similarly feasible, is adiabatic melting of previously subduction-modified (metasomatized) mantle (e.g., Richards, 2009; van Hinsbergen et al., 2020) beneath the study area caused by asthenospheric upwelling and plate margin extension. Furthermore, the lack of a coeval accretionary prism hampers suggesting a straightforward link to a subduction setting at these latitudes as previously suggested. Also, the anomalous isotopic characteristics and the anorogenic nature of the La Estrella granite are not easily reconciled with a typical subduction environment. An alternative hypothesis attuned with these observations, and with the along-strike segmentation in magma composition observed from northern Chile to the study area, is the formation of a Late Triassic-Early Jurassic slab gap (G. Gianni et al., 2019; Rossel et al., 2020) (Figure 7). This explanation was suggested based on two different lines of evidence: (a) one on the surface, linked to the presence of anomalous magmatism and metamorphism in the intraplate Neuquén basin compatible with slab-tearing settings (Figure 1a), and the other (b) on the mantle, where seismic tomography data indicated the existence of a relict slab gap at mid-to-lower mantle depths (G. Gianni et al., 2019; Rossel et al., 2020; Suárez & González, 2018) (Figure 7). However, a tectonomagmatic plate margin record of this slab tearing event has not been documented so far. This record is important because documentation of near-margin magmatism provides the most reliable indicator of slab gap formation in active margins (De Long et al., 1979; G. M. Gianni & Luján, 2021; Groome & Thorkelson, 2009; Marshak & Karig, 1977; Sisson et al., 2003, for a recent synthesis).

A tomotectonic analysis linking the mantle structure corresponding to the Late Triassic subducted slab configurations with the plate margin area analyzed in this study shed light into the possible origin of the ~220–210 Ma granites. This tomotectonic analysis shows a high-velocity vote map stacking 24 global seismic tomography models at 2,100 and 1,700 km (Figure 7a), representing the distribution of subducted lithosphere at ~210 and 170 Ma, respectively (high-vote count areas) considering an average lower mantle slab sinking rate of 1 cm/yr, which is identical to optimal values determined in previous studies (e.g., G. Gianni et al., 2019; Sigloch & Mihalynuk, 2013) (see Supporting Information S1 for further details on tomotectonic analysis methods and seismic tomography models used). Vote maps allow a straightforward comparison across analyzed global seismic tomography models and high-vote count areas allow the detection of reliable high-velocity zones commonly interpreted as subducted slabs (Shephard et al., 2017). To link the southwestern Pangea plate margin in the Late Triassic with the mantle slab records examined in vote maps, we overlapped the Paleozoic-Mesozoic plate-kinematic reconstruction of Mathews et al. (2016) (see Supporting Information S1 for further details). This analysis confirms a spatial coincidence of the reconstructed southwestern margin of Pangea (Mathews et al., 2016) and a fringe of subducted slabs indicated by high-vote counts (Figure 7). Most importantly, this analysis highlights a major discontinuity in the high-vote count fringe coinciding with the reconstructed position of the study area, which was previously interpreted as a Late Triassic slab gap (G. Gianni et al., 2019) (Figure 7). Notably, our new analysis including a large number of seismic tomography models allow us to detect a slab gap covering a more extensive area than previously acknowledged (G. Gianni et al., 2019; Rossel et al., 2020). This subduction discontinuity was later recovered in the Jurassic as illustrated by our tomotectonic reconstruction at 170 Ma depicting high vote counts at 1,700 km that indicate mid-Late Jurassic slab material beneath the study area (Figure 7). We propose that the hot asthenosphere welling up through the slab gap suggested in previous studies not only impacted the intraplate area in the Neuquén Basin (G. Gianni et al., 2019; Rossel et al., 2020), but also the plate margin area coinciding with the current Coastal Cordillera of Central Chile (Figure 7). The slab-tearing would have triggered asthenospheric upwelling (e.g., Rosenbaum et al., 2008; Schellart, 2010) that decompressed a formerly metasomatized mantle source producing basaltic underplating beneath the near-trench plate margin. The latter would have caused partial melting of the metasedimentary Paleozoic subduction complexes and mixed with it to produce high-silica S/I- and S-Type granites of the Constitución and Hualpén and anorogenic granitoids of the Cobquecura area. During

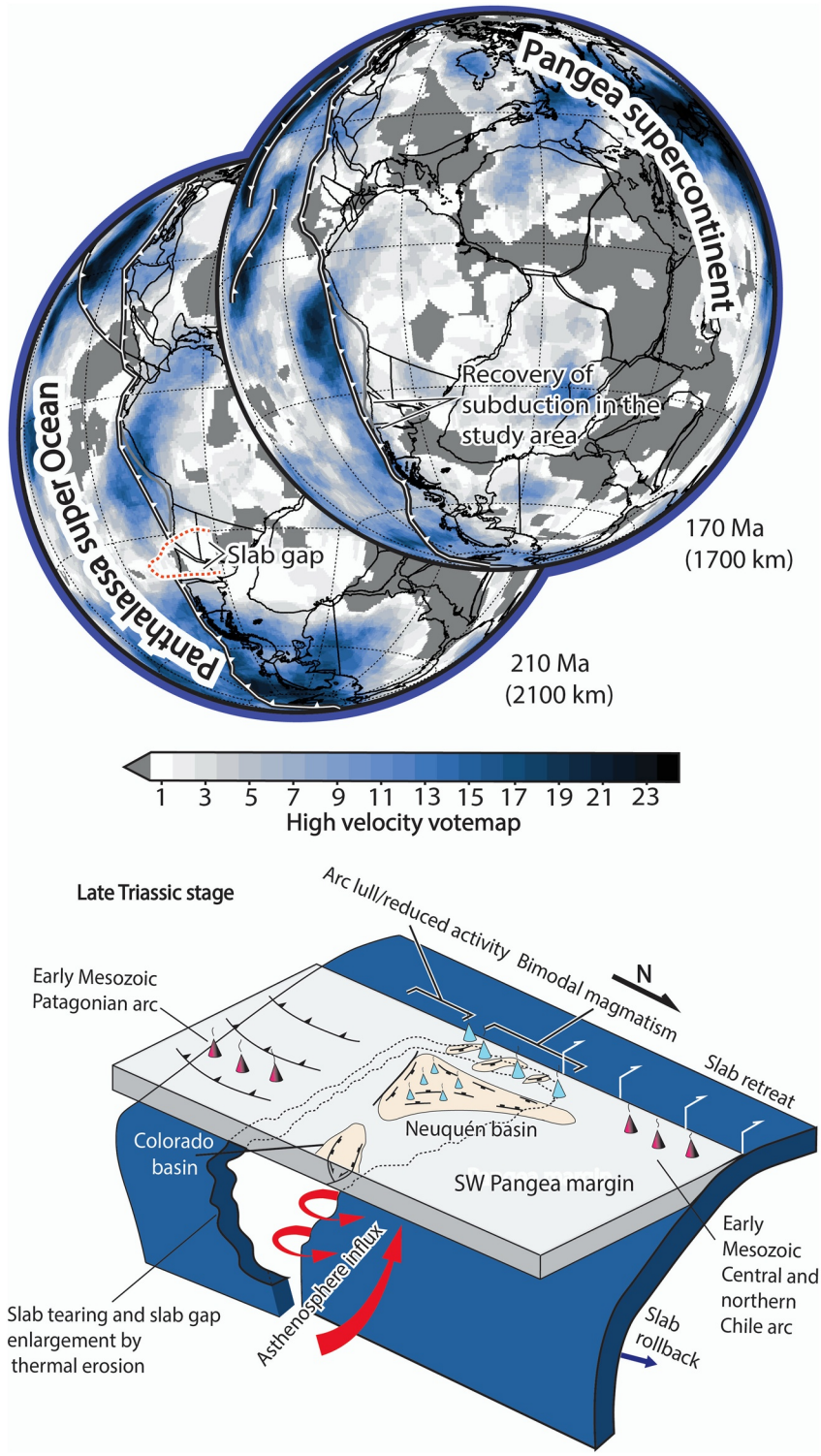

Figure 7.

this process, melting of continental forearc crust that suffered previous hydrothermal alteration at high temperatures along with metasomatized asthenospheric mantle could have jointly generated high-silica magmas with low $\delta^{18}O$ (Guo et al., 2019), high isotopic lead values and CHUR-like $^{87}Sr/^{86}Sr$ and $^{143}Nd/^{144}Nd$ ratios, that would have evolved into the La Estrella Granite (Figures 2 and 4). This process could explain subtle subduction-related

geochemical signatures in the Late Triassic granitoids as resulting from geochemical inheritance caused by the melting of metasedimentary and/or crystalline basements with arc signatures in an anomalous subduction-related scenario. In this context, it is also possible to reinterpret, mantle-derived magmas from the Cobquecura area with subtle magmatic arc geochemical signatures as produced by decompression melting of a previously metasomatized mantle wedge, as recently documented in the Papua New Guinea belt (van Hinsbergen et al., 2020), during slab tear-related mantle upwelling (Schellart, 2010).

We suggest that the Late Triassic magmatism of Southern Central Chile is the western plate-margin counterpart of the slab tear-related magmatism in the intraplate Neuquén Basin previously documented by Gianni et al. (2019) and Rossel et al. (2020) (Figure 1a). Therefore, we propose an origin for the analyzed granitoids directly related to the Late Triassic slab tear and suggest that the observed compositional heterogeneities are the result of a series of tectonomagmatic processes triggered by this major geodynamic event. The rupture and subsequent slab retreat of the slab to the north, would have generated a NNE to SSW tensional regime for early depocenters of the Neuquén and Colorado basin (G. Gianni et al., 2019; Hernández et al., 2021). Plate margin extension in the study area is evidenced by the documentation of a series of extensional Upper Triassic NW-SE to NNW-SSE-oriented depocenters (Charrier et al., 2007; Hervé et al., 1976), which are spatially related to the anorogenic magmatism analyzed in this study (Hervé et al., 1976; Vásquez & Franz, 2008) (Figure 1b). The fact that Late Triassic intraplate extension and the associated magmatism in the Neuquén basin are closely related in time and space with the tectonomagmatic events in the study area in the westernmost plate margin area indicates a common origin directly linked to major changes in the subduction zone at this time. Hence, convergent margin processes may have not been a second-order process in the tectonic evolution of the southwestern Pangea margin as recently suggested by Fennell et al. (2020). By following Navarrete et al. (2019), Fennell et al. (2020) suggested that intraplate extension east of the study area in the Neuquén basin was related to the N-S absolute motion of Gondwana in the Early Jurassic. Nevertheless, this hypothesis does not explain the finding of slab-tear-related magmatism in the synrift basin infill (G. Gianni et al., 2019; Rossel et al., 2020). Instead, we suggest that the fortuitous co-occurrence of major changes in the convergent margin and the absolute upper-plate motion away from the trench, likely acting on a weak structural template inherited from the Gondwanic orogeny, would have jointly acted to drive intense magmatic activity and extensional deformation in this area of southwestern Pangea.

Slab-tearing processes are relatively easier to document in Cenozoic convergent margins, where the upper-plate record is largely preserved, and geophysical tools illuminate segmentations and related slab gaps while still subducting in the upper mantle (e.g., Govers & Wortel, 2005; Rosenbaum et al., 2008, 2019). However, gathering such key information from ancient convergent margins, where the geological record is often incomplete and ancient slabs are now deeply subducted, is challenging. With the now complete upper plate record of the slab-tearing event, spanning the plate margin (this study) to the intraplate area (G. Gianni et al., 2019; Rossel et al., 2020), along with the confirmation of a lower mantle slab gap, the Late Triassic slab-tear event in the southwestern margin of Pangea is undoubtedly the most robustly constrained pre-Cenozoic slab tearing-process so far.

6. Conclusion

The Late Triassic intrusive activity in the Coastal Cordillera of Southern Central Chile is characterized by a series of dominantly high-silica epizonal granitoids. The igneous bodies studied here show highly heterogeneous compositions characterized by the presence of the S-type Hualpén Stock, S/I type Constitución Granite, and A-type La Estrella and Cobquecura granites. Our results indicate that these igneous rocks were intruded in a short time span constrained between ~220 and ~210 Ma during a complex tectonomagmatic process. The updated geochronological, geochemical, and multi-isotopic data, indicative of a short-lived magmatic event with sources from the upper plate (mostly middle/lower crust) influenced by mantle derived melts, along with new

Figure 7. Above is a tomotectonic analysis showing two high-velocity vote map stacking 24 global seismic tomography models at 2,100 and 1,700 km representing the distribution of subducted lithosphere at ~210 and 170 Ma, respectively (high-vote count areas) considering a lower mantle slab sinking rate of 1 cm/yr (G. Gianni et al., 2019; Sigloch & Mihalynuk, 2013). Overlapped is a plate reconstruction of Pangea from Mathews et al. (2016) showing a coincidence of the western margin of Pangea and a fringe of subducted slabs indicated by a high-vote count. In the dashed red line, we highlight an interruption in the fringe of high-vote count areas representative of a subduction discontinuity at 210 Ma beneath the reconstructed position of the study area that was recovered later as illustrated by the reconstruction at 170 Ma. Below is an interpretation of the tomotectonic analysis based on Gianni et al. (2019) and Rossel et al. (2020) where Late Triassic bimodal magmatism in the Coastal Cordillera is here interpreted as resulting from a slab tear that segmented the plate margin at this time. The slab gap separated a region with active subduction-related magmatism south of the study area in Patagonia (Navarrete et al., 2019) and to the north in central to northern Chile (e.g., Oliveros, Creixell, et al., 2020, Oliveros, Moreno-Yaeger, & Flores, 2020).

tomotectonic reconstructions showing a wide area without mantle subduction records, require a reconsideration of previous tectonomagmatic models. We propose that the new data and observations from the Upper Triassic granitoids of the Coastal Cordillera are compatible with a massive slab-tearing episode in the study area. Thus, these granitoids constitute the missing plate margin magmatic record commonly linked to slab tear or slab window processes and complement previous observations in the Patagonian continental interior. The slab-tearing and the resulting slab gap would have triggered a thermal anomaly that induced partial melting of a previously metasomatized asthenospheric mantle and part of the metasedimentary Paleozoic subduction complexes. This resulted in producing high-silica S/I- and S-Type granites of the Constitución and Hualpén granites, and anorogenic granitoids of Cobquecura area. Furthermore, low degrees of melting of continental crust that suffered previous hydrothermal alteration at high temperatures along with metasomatized asthenospheric mantle could have generated high-silica magmas with low $\delta^{18}O$, high Pb isotope values and CHUR-like $^{87}Sr/^{86}Sr$ and $^{143}Nd/^{144}Nd$ ratios, that subsequently evolved into the La Estrella Granite. This process could explain the existence of magmatic arc-like signatures without a typical subduction system, challenging interpretations of previous studies. As there is no record of Triassic accretionary complexes in the study area (Willner et al., 2005), arguments favoring an active Late Triassic subduction process based on their claimed existence are not sustained. Finally, we suggest that the slab-tearing event in south Western Pangea constitutes the most robustly constrained case for a pre-Cenozoic slab tear with a complete plate margin-to-intraplate magmatic record in the upper plate and a slab gap in the deeply subducted lower plate.

Data Availability Statement

Whole rock geochemical and isotopical data used in this study is available at Rossel (2022a). SHRIMP U/Pb, Lu-Hf and Oxygen zircon data used in this study is available at Rossel (2022b).

Acknowledgments
This study was funded through the FONDECYT Iniciación Grant 11160329 (Pablo Rossel). Francisco Carvajal is thanked for assistance in the fieldwork. Guido M. Gianni acknowledges the support of CONICET and the University of San Juan. Mihai N. Ducea acknowledges support from the Romanian Executive Agency for Higher Education, Romanian MCID Grant: C1.2.PFE-CDI.2021-587/ Contract no.41PFE/30.12.2021, Research, Development and Innovation Funding project, PN-III-P4-ID-PCCF-2016-0014. The editor, of the Journal and the reviewers Feng Guo, Verónica Oliveros and Suzanne Kay are especially thanked by their highly constructive comments and suggestions.

References

Alasino, P. H., Paterson, S. R., Kirsch, M., & Larrovere, M. A. (2022). The role of crustal thickness on magma composition in arcs: An example from the pre-Andean, South American Cordillera. *Gondwana Research*, *106*, 191–210. https://doi.org/10.1016/j.gr.2022.01.009

Annen, C., Blundy, J. D., & Sparks, R. S. J. (2006). The genesis of intermediate and silicic magmas in deep crustal hot zones. *Journal of Petrology*, *47*(3), 505–539. https://doi.org/10.1093/petrology/egi084

Antunes, I., Neiva, A., Silva, M., & Corfu, F. (2008). Geochemistry of S-type granitic rocks from the reversely zoned Castelo Branco pluton (central Portugal). *Lithos*, *103*(3–4), 445–465. https://doi.org/10.1016/j.lithos.2007.10.003

Appleby, S., Gillespie, M., Graham, C., Hinton, R., Oliver, G., & Kelly, N., & EIMF. (2010). Do S-type granites commonly sample infracrustal sources? New results from an integrated O, U–Pb and Hf isotope study of zircon. *Contributions to Mineralogy and Petrology*, *160*(1), 115–132. https://doi.org/10.1007/s00410-009-0469-3

Bouvier, A., Vervoort, J., & Patchett, P. (2008). The Lu–Hf and Sm–Nd isotopic composition of CHUR: Constraints from unequilibrated chondrites and implications for the bulk composition of terrestrial planets. *Earth and Planetary Science Letters*, *273*(1–2), 48–57. https://doi.org/10.1016/j.epsl.2008.06.010

Chappell, B., & White, A. (1974). Two contrasting granite types. *Pacific Geology*, *8*, 173–174.

Charrier, R. (1979). El Triásico en Chile y regiones adyacentes de Argentina: Una reconstrucción paleogeográfica y paleoclimática. *Comunicaciones*, *26*, 1–37.

Charrier, R., Pinto, L., & Rodríguez, M. P. (2007). Tectonostratigraphic evolution of the Andean Orogen in Chile. In T. Moreno & W. Gibbons (Eds.), *The geology of Chile* (pp. 21–114). Geological Society, London, Special Publications. https://doi.org/10.1144/goch.3

Clemens, J., & Vielzeuf, D. (1987). Constraints on melting and magma production in the crust. *Earth and Planetary Science Letters*, *86*(2–4), 287–306. https://doi.org/10.1016/0012-821x(87)90227-5

Cocchi, L., Passaro, S., Tontini, F. C., & Ventura, G. (2017). Volcanism in slab tear faults is larger than in island-arcs and back-arcs. *Nature Communications*, *8*(1), 1–12. https://doi.org/10.1038/s41467-017-01626-w

Collins, W., Beams, S., White, A., & Chappell, B. (1982). Nature and origin of A-type granites with particular reference to southeastern Australia. *Contributions to Mineralogy and Petrology*, *80*(2), 189–200. https://doi.org/10.1007/bf00374895

Coloma, F., Valin, X., Oliveros, V., Vásquez, P., Creixell, C., Salazar, E., & Ducea, M. (2017). Geochemistry of Permian to Triassic igneous rocks from northern Chile (28°–30°15′S): Implications on the dynamics of the proto-Andean margin. *Andean Geology*, *44*(2), 147–178. https://doi.org/10.5027/andgeoV44n2-a03

Dávila, A., Hervé, F., & Munizaga, F. (1979). Edades K/Ar en granitoides de la Cordillera de la Costa de la provincia de Colchagua, VI Región, Chile central. In *2nd Congreso Geológico Chileno (Puerto Varas, 1979)* (pp. F107–F120).

Deckart, K., Herve, F., Fanning, C. M., Ramírez, V., Calderon, M., & Godoy, E. (2014). U-Pb geochronology and Hf-O isotopes of zircons from the Pennsylvanian coastal batholith, south-Central Chile. *Andean Geology*, *41*, 49–82. https://doi.org/10.5027/andgeoV41n1-a03

De Long, S. E., Schwarz, W. M., & Anderson, R. N. (1979). Thermal effects of ridge subduction Earth Planet. *Science Letter*, *44*(2), 239–246. https://doi.org/10.1016/0012-821x(79)90172-9

del Rey, Á., Deckart, K., Arriagada, C., & Martínez, F. (2016). Resolving the paradigm of the late Paleozoic–Triassic Chilean magmatism: Isotopic approach. *Gondwana Research*, *37*, 172–181. https://doi.org/10.1016/j.gr.2016.06.008

del Rey, Á., Deckart, K., Planavsky, N., Arriagada, C., & Martínez, F. (2019). Tectonic evolution of the southwestern margin of Pangea and its global implications: Evidence from the mid Permian–Triassic magmatism along the Chilean-Argentine border. *Gondwana Research*, *76*, 303–321. https://doi.org/10.1016/j.gr.2019.05.007

Espinoza, M., Montecino, D., Oliveros, V., Astudillo, N., Vásquez, P., Reyes, R., et al. (2019). The synrift phase of the early Domeyko Basin (Triassic, northern Chile): Sedimentary, volcanic and tectonic interplay in the evolution of an ancient subduction-related rift basin. *Basin Research*, *31*(1), 4–32. https://doi.org/10.1111/bre.12305

Faccenna, C., Funiciello, F., Civetta, L., D'Antonio, M., Moroni, M., & Piromallo, C. (2007). Slab disruption, mantle circulation, and the opening of the Tyrrhenian basins. In L. Beccaluva, G. Bianchini, & M. Wilson (Eds.), *Cenozoic volcanism in the Mediterranean area: Geological Society of America special Paper 418* (pp. 153–169). https://doi.org/10.1130/2007.2418(08)

Faure, G. (1986). *Principles of isotope geochemistry* (p. 464). JohnWiley.

Fennell, L. M., Naipauer, M., Borghi, P., Sagripanti, L., Pimentel, M., & Folguera, A. (2020). Early Jurassic intraplate extension in west-central Argentina constrained by U-Pb SHRIMP dating: Implications for the opening of the Neuquén basin. *Gondwana Research*, *87*, 278–302. https://doi.org/10.1016/j.gr.2020.06.017

Finger, F., & Schiller, D. (2012). Lead contents of S-type granites and their petrogenetic significance. *Contributions to Mineralogy and Petrology*, *164*(5), 747–755. https://doi.org/10.1007/s00410-012-0771-3

Franzese, J. R., & Spalletti, L. A. (2001). Late Triassic-early Jurassic continental extension in southwestern Gondwana: Tectonic segmentation and pre-break-up rifting. *Journal of South American Earth Sciences*, *14*(3), 257–270. https://doi.org/10.1016/S0895-9811(01)00029-3

Gana, P., & Hervé, F. (1983). Geología del basamento cristalino de la Cordillera de la Costa entre los ríos Mataquito y Maule, VII Región. *Revista Geologica de Chile*, *19*, 37–56.

Georgieva, V., Gallagher, K., Sobczyk, A., Sobel, E. R., Schildgen, T. F., Ehlers, T. A., & Strecker, M. R. (2019). Effects of slab-window, alkaline volcanism, and glaciation on thermochronometer cooling histories, Patagonian Andes. *Earth and Planetary Science Letters*, *511*, 164–176. https://doi.org/10.1016/j.epsl.2019.01.030

Gianni, G., Navarrete, C., & Spagnotto, S. (2019). Surface and mantle records reveal an ancient slab tear beneath Gondwana. *Scientific Reports*, *9*(1), 1–10. https://doi.org/10.1038/s41598-019-56335-9

Gianni, G. M., & Luján, S. P. (2021). Geodynamic controls on magmatic arc migration and quiescence. *Earth-Science Reviews*, *218*, 103676. https://doi.org/10.1016/j.earscirev.2021.103676

Gianni, G. M., & Navarrete, C. R. (2022). Catastrophic slab loss in southwestern Pangea preserved in the mantle and igneous records. *Nature Communications*, *13*(1), 698. https://doi.org/10.1038/s41467-022-28290-z

Goodge, J., & Vervoort, J. (2006). Origin of Mesoproterozoic A-type granites in Laurentia: Hf isotope evidence. *Earth and Planetary Science Letters*, *243*(3–4), 711–731. https://doi.org/10.1016/j.epsl.2006.01.040

Govers, R., & Wortel, M. J. R. (2005). Lithosphere tearing at STEP faults: Response to edges of subduction zones. *Earth and Planetary Science Letters*, *236*(1–2), 505–523. https://doi.org/10.1016/j.epsl.2005.03.022

Groome, W. G., & Thorkelson, D. J. (2009). The three-dimensional thermomechanical signature of ridge subduction and slab window migration Tectonophysics. *Tectonophysics*, *464*(1–4), 70–83. https://doi.org/10.1016/j.tecto.2008.07.003

Guillaume, B., Funiciello, F., Faccenna, C., Martinod, J., & Olivetti, V. (2010). Spreading pulses of the Tyrrhenian Sea during the narrowing of the Calabrian slab. *Geology*, *38*(9), 819–822. https://doi.org/10.1130/g31038.1

Guo, F., Huang, M., & Zhao, L. (2019). Nd-Hf-O isotopic evidence for subduction-induced crustal replacement in NE China. *Chemical Geology*, *525*, 125–142. https://doi.org/10.1016/j.chemgeo.2019.07.013

Guo, F., Wu, Y. M., Zhang, B., Zhang, X. B., Zhao, L., & Liao, J. (2021). Magmatic responses to Cretaceous subduction and tearing of the paleo-Pacific Plate in SE China: An overview. *Earth-Science Reviews*, *212*, 103448. https://doi.org/10.1016/j.earscirev.2020.103448

Hernández, N. M., Galetto, A., Cristallini, E. O., García, V. H., Bechis, F., & Giambiagi, L. B. (2021). Late Triassic-Early Jurassic extensional tectonics in the Neuquén Basin (Argentina). New insights from stratigraphic and structural analyses of the Chachil depocenter (39°S). *Journal of Structural Geology*, *154*, 104483. https://doi.org/10.1016/j.jsg.2021.104483

Hervé, F., Calderón, M., Fanning, C. M., Pankhurst, R. J., & Godoy, E. (2013). Provenance variations in the Late Paleozoic accretionary complex of central Chile as indicated by detrital zircons. *Gondwana Research*, *23*(3), 1122–1135. https://doi.org/10.1016/j.gr.2012.06.016

Hervé, F., Fanning, C. M., Calderón, M., & Mpodozis, C. (2014). Early Permian to Late Triassic batholiths of the Chilean Frontal Cordillera (28°–31°S): SHRIMP U–Pb zircon ages and Lu–Hf and O isotope systematics. *Lithos*, *184–187*, 436–446. https://doi.org/10.1016/j.lithos.2013.10.018

Hervé, F., Kawashita, K., Munizaga, F., & Bassei, M. (1984). Rb/Sr isotopic ages from late Paleozoic metamorphic rocks of central Chile. *Journal of the Geological Society of London*, *141*(5), 877–884. https://doi.org/10.1144/gsjgs.141.5.0877

Hervé, F., & Munizaga, F. (1978). Evidencias geocronológicas de un magmatismo intrusivo Triásico Superior–Jurásico en la Cordillera de la Costa de Chile entre los 35°30′S y 36°30′S. *7th Congreso Geológico Argentino. (Neuquén, 1978)*, *2*, 43–52.

Hervé, F., Munizaga, F., Parada, M. A., Brook, M., Pankhurst, R., Snelling, N., & Drake, R. (1988). Granitoids of the Coast Range of central Chile: Geochronology and geologic setting. *Journal of South American Earth Sciences*, *1*(2), 185–194. https://doi.org/10.1016/0895-9811(88)90036-3

Hervé, F., Thiele, R., & Parada, M. A. (1976). Observaciones geológicas en el Triásico de Chile central entre las latitudes 35°30′ y 40°00′ sur. *I Congreso Geologico Chileno Santiago, Actas 1A*, 297–313.

Howell, J. A., Schwarz, E., Spalletti, L. A., & Veiga, G. D. (2005). The Neuquen basin: An overview. *Geological Society, London, Special Publications*, *252*, 1–14. https://doi.org/10.1144/GSL.SP.2005.252.01.01

Hu, J., & Liu, L. (2016). Abnormal seismological and magmatic processes controlled by the tearing South American flat slabs. *Earth and Planetary Science Letters*, *450*, 40–51. https://doi.org/10.1016/j.epsl.2016.06.019

Jacques, G., Hoernle, K., Gill, J., Hauff, F., Wehrmann, H., Garbe-Schönberg, D., et al. (2013). Across-arc geochemical variations in the Southern Volcanic Zone, Chile (34.5°–38.0°S): Constraints on mantle wedge and slab input compositions. *Geochimica et Cosmochimica Acta*, *123*, 218–243. https://doi.org/10.1016/j.gca.2013.05.016

Jolivet, L., Menant, A., Sternai, P., Rabillard, A., Arbaret, L., Augier, R., et al. (2015). The geological signature of a slab tear below the Aegean. *Tectonophysics*, *659*, 166–182. https://doi.org/10.1016/j.tecto.2015.08.004

Kay, S. M. (1993). Late Paleozoic tectonics in Southern South America: A global perspective. In *XII International Congress on Carboniferous Permian, Comptes Rendus* (Vol. 1, pp. 109–122).

Kay, S. M., Ramos, V. A., Mpodozis, C., & Sruoga, P. (1989). Late Paleozoic to Jurassic silicic magmatism at the Gondwana margin: Analogy to the Middle Proterozoic in North America? *Geology*, *17*(4), 324–328. https://doi.org/10.1130/0091-7613(1989)017<0324:lptjsm>2.3.co;2

Le Breton, N., & Thompson, A. (1988). Fluid-absent (dehydration) melting of biotite in metapelites in the early stages of crustal anatexis. *Contributions to Mineralogy and Petrology*, *99*(2), 226–237. https://doi.org/10.1007/bf00371463

Lucassen, F., Trumbull, R., Franz, G., Creixell, C., Vásquez, P., Romer, R. L., & Figueroa, O. (2004). Distinguishing crustal recycling and juvenile additions at active continental margins: The Paleozoic to recent compositional evolution of the Chilean Pacific margin (36°–41°S). *Journal of South American Earth Sciences*, *17*(2), 103–119. https://doi.org/10.1016/j.jsames.2004.04.002

Lynen, R. L., & Cuney, M. (2005). Granite-related rare-element deposits and experimental constraints on Ta-Nb-W-Sn-Zr-Hf mineralization. In R. L. Linnen & I. M. Samson (Eds.), *Rare-element geochemistry and mineral deposits* (Vol. 17, pp. 45–68). Geological Association of Canada Short Course Notes.

Maksaev, V., Munizaga, F., & Tassinari, C. (2014). Timing of the magmatism of the paleo-Pacific border of Gondwana: U–Pb geochronology of Late Paleozoic to Early Mesozoic igneous rocks of the north Chilean Andes between 20° and 31°S. *Andean Geology*, *41*(3), 447–506. https://doi.org/10.5027/andgeoV41n3-a01

Marshak, R. S., & Karig, D. E. (1977). Triple junctions as a cause for anomalously near-trench igneous activity between the trench and volcanic arc. *Geology*, *5*(4), 233–236. https://doi.org/10.1130/0091-7613(1977)5<233:tjaacf>2.0.co;2

Mathews, K. J., Maloney, K. T., Zahirovic, S., Williams, S. E., Seton, M., & Mueller, R. D. (2016). Global plate boundary evolution and kinematics since the late Paleozoic. *Global and Planetary Change*, *146*, 226–250. https://doi.org/10.1016/j.gloplacha.2016.10.002

Mpodozis, C., & Kay, S. M. (1992). Late Paleozoic to Triassic evolution of the Gondwana margin: Evidence from Chilean Frontal cordilleran batholiths (28°S to 31°S). *The Geological Society of America Bulletin*, *104*(8), 999–1014. https://doi.org/10.1130/0016-7606(1992)104<0999:LPTTEO>2.3.CO;2

Navarrete, C., Gianni, G., Encinas, A., Márquez, M., Kamerbeek, Y., Valle, M., & Folguera, A. (2019). Triassic to Middle Jurassic geodynamic evolution of southwestern Gondwana: From a large flat-slab to mantle plume suction in a rollback subduction setting. *Earth-Science Reviews*, *194,* 125–159. https://doi.org/10.1016/j.earscirev.2019.05.002

Oliveros, V., Creixell, C., Vásquez, P., Lucassen, F., Ducea, M. N., Ciocca, I., et al. (2020). Lithospheric evolution of the Pre- and Early Andean convergent margin. Chile. *Gondwana Research*, *80*, 202–227. https://doi.org/10.1016/j.gr.2019.11.002

Oliveros, V., Moreno-Yaeger, P., & Flores, L. (2020). Igneous Rock Associations 25. Pre-Pliocene Andean Magmatism in Chile. *Geoscience Canada: Journal of the Geological Association of Canada/Geoscience Canada: journal de l'Association Géologique du Canada*, *47*(1–2), 65–82. https://doi.org/10.12789/geocanj.2020.47.158

Pearce, J., Harris, B., & Tindle, A. (1984). Trace element discrimination diagrams for the tectonic interpretation of granitic rocks. *Journal of Petrology*, *25*(4), 956–983. https://doi.org/10.1093/petrology/25.4.956

Poole, G., Kemp, A., Hagemann, S., Fiorentini, M., Jeon, H., Williams, I., et al. (2020). The petrogenesis of back-arc magmas, constrained by zircon O and Hf isotopes, in the Frontal Cordillera and Precordillera, Argentina. *Contributions to Mineralogy and Petrology*, *175*(9), 89. https://doi.org/10.1007/s00410-020-01721-0

Ramos, V. A., & Kay, S. M. (1991). Triassic rifting and associated basalts in the Cuyo basin, central Argentina. In R. S. Harmon & C. W. Rapela (Eds.), *Andean magmatism and its tectonic setting* (Vol. 265, pp. 79–91). Geological Society of America, Special Publications.

Rapela, C., Pankhurst, R., Casquet, C., Dahlquist, J., Fanning, C., Baldo, E., et al. (2018). A review of the Famatinian ordovician magmatism in southern South America: Evidence of lithosphere reworking and continental subduction in the early proto-Andean margin of Gondwana. *Earth-Sciences Reviews*, *187*, 259–285. https://doi.org/10.1016/j.earscirev.2018.10.006

Richards, J. P. (2009). Postsubduction porphyry Cu-Au and epithermal Au deposits: Products of remelting of subduction-modified lithosphere. *Geology*, *37*(3), 247–250. https://doi.org/10.1130/g25451a.1

Rosenbaum, G., Gasparon, M., Lucente, F. P., Peccerillo, A., & Miller, M. S. (2008). Kinematics of slab tear faults during subduction segmentation and implications for Italian magmatism. *Tectonics*, *27*(2), TC2008. https://doi.org/10.1029/2007tc002143

Rosenbaum, G., Sandiford, M., Caulfield, J., & Garrison, J. M. (2019). A trapdoor mechanism for slab tearing and melt generation in the northern Andes. *Geology*, *47*(1), 23–26. https://doi.org/10.1130/g45429.1

Rossel, P., Echaurren, A., Ducea, M. N., Maldonado, P., & Llanos, K. (2020). Jurassic segmentation of the early Andean magmatic Province in Southern Central Chile (35–39°S): Petrological constrains and tectonic drivers. *Lithos*, *364–365*, 364–365. https://doi.org/10.1016/j.lithos.2020.105510

Rutland, R. W. R. (1971). Andean orogeny and ocean floor spreading. *Nature*, *233*(5317), 252–255. https://doi.org/10.1038/233252a0

Schellart, W. P. (2010). Mount Etna–Iblean volcanism caused by rollback-induced upper mantle upwelling around the Ionian slab edge: An alternative to the plume model. *Geology*, *38*(8), 691–694. https://doi.org/10.1130/g31037.1

Sernageomin (2003). *Mapa geológico de Chile: Versión digital* (Vol. 4). Servicio Nacional De Geología y Minería, Publicación Geológica Digital.

Shand, S. J. (1947). *The eruptive rocks* (3rd ed., p. 444). John Wiley.

Shephard, G. E., Matthews, K. J., Hosseini, K., & Domeier, M. (2017). On the consistency of seismically imaged lower mantle slabs. *Scientific Reports*, *7*(1), 1–17. https://doi.org/10.1038/s41598-017-11039-w

Siebel, W., & Chen, F. (2009). Zircon Hf isotope perspective on the origin of granitic rocks from eastern Bavaria, SW Bohemian Massif. *International Journal of Earth Sciences*, *99*(5), 993–1005. https://doi.org/10.1007/s00531-009-0442-4

Sigloch, K., & Mihalynuk, M. G. (2013). Intra-oceanic subduction shaped the assembly of Cordilleran North America. *Nature*, *496*(7443), 50–56. https://doi.org/10.1038/nature12019

Sisson, V. B., Pavlis, T. L., Roeske, S. M., & Thorkelson, D. J. (2003). Introduction: An overview of ridge-trench interactions in modern and ancient settings. *Geological Society of America Special Paper*, *371*, 1–18.

Soderlund, U., Patchett, P., Vervoort, J. D., & Isachsen, C. E. (2004). The ^{176}Lu decay constant determined by Lu-Hf and U-Pb isotope systematics of Precambrian mafic intrusions. *Earth and Planetary Science Letters*, *219*(3–4), 311–324. https://doi.org/10.1016/s0012-821x(04)00012-3

Stepanov, A. S., Meffre, S., Mavrogenes, J., & Steadman, J. (2016). Nb-Ta fractionation in peraluminous granites: A marker of the magmatic-hydrothermal transition: COMMENT. *Geology*, *44*(7), e394. https://doi.org/10.1130/g38086c.1

Stevens, G., Clemens, J., & Droop, G. (1997). Melt production during granulite-facies anatexis: Experimental data from "primitive" metasedimentary protoliths. *Contributions to Mineralogy and Petrology*, *128*(4), 352–370. https://doi.org/10.1007/s004100050314

Suárez, R. J., & González, P. D. (2018). Caracterización geológica del metamorfismo diastatermal mesozoico en la Cuenca Neuquina y su relación con la anomalía térmica en el sinrift. *Revista de la Asociación Geológica Argentina*, *75*, 457–472.

Troch, J., Ellis, B., Harris, C., Bachmann, O., & Bindeman, I. (2020). Low-δ^{18}O silicic magmas on Earth: A review. *Earth-Science Reviews*, *208*, 103299. https://doi.org/10.1016/j.earscirev.2020.103299

Valley, J. W., Lackey, J. S., Cavosie, A. J., Clechenko, C. C., Spicuzza, M. J., Basei, M. A. S., et al. (2005). 4.4 Billion years of crustal maturation: Oxygen isotope ratios of magmatic zircon. *Contributions to Mineralogy and Petrology*, *150*(6), 561–580. https://doi.org/10.1007/s00410-005-0025-8

Van der Meer, D. G., Van Hinsbergen, D. J., & Spakman, W. (2018). Atlas of the underworld: Slab remnants in the mantle, their sinking history, and a new outlook on lower mantle viscosity. *Tectonophysics*, *723*, 309–448. https://doi.org/10.1016/j.tecto.2017.10.004

Van der Voo, R., Spakman, W., & Bijwaard, H. (1999). Mesozoic subducted slabs under Siberia. *Nature*, *397*(6716), 246–249. https://doi.org/10.1038/16686

Van Hinsbergen, D. J. J., Spakman, W., de Boorder, H., van Dongen, M., Jowitt, S. M., & Mason, P. R. D. (2020). Arc-type magmatism due to continental edge plowing through ancient subduction-enriched mantle. *Geophysical Research Letters*, *47*(9), e2020GL087484. https://doi.org/10.1029/2020GL087484

Vásquez, P., & Franz, G. (2008). The Triassic Cobquecura Pluton (central Chile): An example of a fayalite-bearing A-type intrusive massif at a continental margin. *Tectonophysics*, *459*(1–4), 66–84. https://doi.org/10.1016/j.tecto.2007.11.067

Vásquez, P., Franz, G., & Frei, D. (2006). Petrology of the Late Triassic arfvedsonite-granitoid at La Estrella (central Chile). In *XI Congreso Geolôgico Chileno (Antofagasta, 2006)* (pp. 573–576).

Vásquez, P., Franz, G., & Wemmer, K. (2005). Fe-rich silicates in the Cobquecura pluton: An indicator of A-type granitoids in the Triassic magmatism of southcentral Chile. In *6th ISAG. Extended Abstracts. Barcelona* (pp. 773–775).

Vásquez, P., Glodny, J., Franz, G., Frei, D., & Romer, R. L. (2011). Early Mesozoic plutonism of the Cordillera de la Costa (34°–37°S), Chile: Constraints on the onset of the Andean Orogeny. *The Journal of Geology*, *119*(2), 159–184. https://doi.org/10.1086/658296

Vásquez, P., Glodny, J., Franz, G., Romer, R. L., & Gerdes, A. (2009). Origin of fayalite granitoids: New insights from the Cobquecura Pluton, Chile, and its metapelitic xenoliths. *Lithos*, *110*(1–4), 181–198. https://doi.org/10.1016/j.lithos.2009.01.001

Vervoort, J., & Blichert-Toft, J. (1999). Evolution of the depleted mantle: Hf isotope evidence from juvenile rocks through time. *Geochemica et Coscochemica acta*, *63*, 533–556.

Vielzeuf, D., & Holloway, J. (1988). Experimental determination of the fluid-absent melting relations in the pelitic system. *Contributions to Mineralogy and Petrology*, *98*(3), 257–276. https://doi.org/10.1007/bf00375178

Vielzeuf, D., & Montel, J. (1994). Partial melting of metagreywackes. Part I. Fluid-absent experiments and phase relationships. *Contributions to Mineralogy and Petrology*, *117*(4), 375–393. https://doi.org/10.1007/bf00307272

Wasserburg, G. J., Jacobsen, S. B., DePaolo, D. J., McCulloch, M. T., & Wen, T. (1981). Precise determination of Sm/Nd ratios, Sm and Nd isotopic abundances in standard solutions. *Geochimica et Cosmochimica Acta*, *45*(12), 2311–2323. https://doi.org/10.1016/0016-7037(81)90085-5

Whalen, J. B., Currie, K. L., & Chappell, B. W. (1987). A-type granite: Geochemical characteristics. Discrimination and petrogenesis. *Contributions to Mineralogy and Petrology*, *95*(4), 407–419. https://doi.org/10.1007/bf00402202

Willner, A. P., Thomson, S. N., Kröner, A., Wartho, J. A., Wijbrans, J. R., & Hervé, F. (2005). Time markers for the evolution and exhumation history of a Late Palaeozoic paired metamorphic belt in North–Central Chile (34–35 30′ S). *Journal of Petrology*, *46*(9), 1835–1858. https://doi.org/10.1093/petrology/egi036

Zhao, L., Guo, F., Zhang, X. B., & Wang, G. Q. (2021). Cretaceous crustal melting records of tectonic transition from subduction to slab rollback of the Paleo-Pacific Plate in SE China. *Lithos*, *384–385*, 105985. https://doi.org/10.1016/j.lithos.2021.105985

Zhou, X.-C., Zhang, H., Guo, L., Yang, H., & Zhong, G. (2021). Petrogenesis of the Early Paleozoic S-type granites in southern Alxa, Northwest China and its implications on fluid flourishing in the middle and lower crust. *Lithos*, *400–401*, 400–401. https://doi.org/10.1016/j.lithos.2021.106363

Zhu, Z., Campbell, I., Allen, C., & Burnham, A. (2020). S-type granites: Their origin and distribution through time as determined from detrital zircons. *Earth and Planetary Science Letters*, *536*, 116140. https://doi.org/10.1016/j.epsl.2020.116140

References From the Supporting Information

Amaru, M. L. (2007). *Global travel time tomography with 3-D reference models* (Vol. 274). Utrecht University.

Black, L. P., Kamo, S. L., Allen, C. M., Aleinikoff, J. N., Davis, D. W., Korsch, R. J., & Foudoulis, C. (2003). TEMORA 1: A new zircon standard for Phanerozoic U-Pb geochronology. *Chemical Geology*, *200*(1–2), 155–170. https://doi.org/10.1016/s0009-2541(03)00165-7

Domeier, M., & Torsvik, T. H. (2014). Plate tectonics in the late Paleozoic. *Geoscience Frontiers*, *5*(3), 303–350. https://doi.org/10.1016/j.gsf.2014.01.002

Drew, S., Ducea, M., & Schoenbohm, L. (2009). Mafic volcanism on the Puna Plateau, NW Argentina: Implications for lithospheric composition and evolution with an emphasis on lithospheric foundering. *Lithosphere*, *1*(5), 305–318. https://doi.org/10.1130/l54.1

Ducea, M. N., & Saleeby, J. B. (1998). The age and origin of a thick mafic ultramafic root from beneath the Sierra Nevada batholiths. *Contributions to Mineralogy and Petrology*, *133*(1–2), 169–185. https://doi.org/10.1007/s004100050445

Durand, S., Debayle, E., Ricard, Y., & Lambotte, S. (2016). Seismic evidence for a change in the large-scale tomographic pattern across the D′′ layer. *Geophysical Research Letters*, *43*(15), 7928–7936. https://doi.org/10.1002/2016gl069650

Eggins, S. M., Grun, R., McCulloch, M. T., Pike, A. W., Chappell, J., Kinsley, L., et al. (2005). In situ U-series dating by laser-ablation multi-collector ICPMS: New prospects for Quaternary geochronology. *Quaternary Science Reviews*, *24*(23–24), 2523–2538. https://doi.org/10.1016/j.quascirev.2005.07.006

Houser, C., Masters, G., Shearer, P., & Laske, G. (2008). Shear and compressional velocity models of the mantle from cluster analysis of long-period waveforms. *Geophysical Journal International*, *174*(1), 195–212. https://doi.org/10.1111/j.1365-246x.2008.03763.x

Hosseini, K., Matthews, K. J., Sigloch, K., Shephard, G. E., Domeier, M., & Tsekhmistrenko, M. (2018). SubMachine: Web-based tools for exploring seismic tomography and other models of Earth's deep interior. *Geochemistry, Geophysics, Geosystems*, *19*(5), 1464–1483. https://doi.org/10.1029/2018gc007431

Hosseini, K., Sigloch, K., Tsekhmistrenko, M., Zaheri, A., Nissen-Meyer, T., & Igel, H. (2020). Global mantle structure from multifrequency tomography using P, PP and P-diffracted waves. *Geophysical Journal International*, *220*(1), 96–141. https://doi.org/10.1093/gji/ggz394

Ickert, R. B., Hiess, J., Williams, I. S., Holden, P., Ireland, T. R., Lanc, P., et al. (2008). Determining high precision, in situ, oxygen isotope ratios with a SHRIMP II: Analyses of MPI-DING silicate-glass reference materials and zircon from contrasting granites. *Chemical Geology*, *257*(1–2), 114–128. https://doi.org/10.1016/j.chemgeo.2008.08.024

Li, C., van der Hilst, R. D., Engdahl, E. R., & Burdick, S. (2008). A new global model for P wave speed variations in Earth's mantle. *Geochemistry, Geophysics, Geosystems*, *9*(5), Q05018. https://doi.org/10.1029/2007gc001806

Lu, C., Grand, S. P., Lai, H., & Garnero, E. J. (2019). TX2019slab: A new P and S tomography model incorporating subducting slabs. *Journal of Geophysical Research: Solid Earth*, *124*(11), 11549–11567. https://doi.org/10.1029/2019jb017448

Ludwig, K. R. (2001). *Squid 1.00. A user's manual*. Berkeley Geochronology Center Special Publication.

Ludwig, K. R. (2003). *Isoplot 3.00: A geochronological toolkit for Microsoft Excel* (p. 70). Berkeley Geochronology Center.

Montelli, R., Nolet, G., Dahlen, F. A., & Masters, G. (2006). A catalogue of deep mantle plumes: New results from finite-frequency tomography. *Geochemistry, Geophysics, Geosystems*, *7*(11), Q11007. https://doi.org/10.1029/2006gc001248

Munizaga, F., Maksaev, V., Fanning, C. M., Giglio, S., Yaxley, G., & Tassinari, C. C. G. (2008). Late Paleozoic–Early Triassic magmatism on the western margin of Gondwana: Collahuasi area, Northern Chile. *Gondwana Research*, *13*(3), 407–427. https://doi.org/10.1016/j.gr.2007.12.005

Müller, R. D., Cannon, J., Qin, X., Watson, R. J., Gurnis, M., Williams, S., et al. (2018). GPlates: Building a virtual Earth through deep time. *Geochemistry, Geophysics, Geosystems*, *19*(7), 2243–2261. https://doi.org/10.1029/2018gc007584

Otamendi, J. E., Ducea, M. N., Tibaldi, A. M., Bergantz, G., de la Rosa, J. D., & Vujovich, G. I. (2009). Generation of tonalitic and dioritic magmas by coupled partial melting of gabbroic and metasedimentary migmatites in the deep crust of the Famatinian arc Argentina. *Journal of Petrology*, *50*(5), 841–873. https://doi.org/10.1093/petrology/egp022

Paces, J. B., & Miller, J. D. (1993). Precise U-Pb ages of Duluth complex and related mafic intrusions, northeastern Minnesota: Geochronological insights to physical, petrogenetic, paleomagnetic, and tectonomagmatic processes associated with the 1.1 Ga midcontinental rift system. *Journal of Geophysical Research*, *98*(B8), 13997–14013. https://doi.org/10.1029/93jb01159

Paton, C., Hellstrom, J., Paul, B., Woodhead, J., & Hergt, J. (2011). Iolite: Freeware for the visualisation and processing of mass spectrometric data. *J Anal At Spectrom*, *26*(12), 2508–2518. https://doi.org/10.1039/c1ja10172b

Rossel, P. (2022a). GQ of Upper Triassic granites of Central Chile. Mendeley Data, V1. https://doi.org/10.17632/8g7j6zf5g7.1

Rossel, P. (2022b). SHRIMP Data of Upper Triassic granites of Southern Central Chile. Mendeley Data, V1. https://doi.org/10.17632/yfyzc25jgw.1

Sláma, J., Kosler, J., Condon, D. J., Crowley, J. L., Gerdes, A., Hanchar, J. M., et al. (2008). Plešovice zircon – A new natural reference material for U-Pb and Hf isotopic microanalysis. *Chemical Geology*, *249*(1–2), 1–35. https://doi.org/10.1016/j.chemgeo.2007.11.005

Williams, I. S. (1998). U-Th-Pb geochronology by ion microprobe. In M. A. McKibben, W. C. Shanks, & W. I. Ridley (Eds.), *Application of microanalytical techniques to understanding mineralizing processes* (Vol. 7, pp. 1–35). Society of Economic Geologists, Reviews of Economic Geology.

Woodhead, J. D., & Hergt, J. M. (2005). A preliminary appraisal of seven natural zircon reference materials for in situ Hf isotope determination. *Geostandards and Geoanalytical Research*, *29*(2), 183–195. https://doi.org/10.1111/j.1751-908x.2005.tb00891.x